

# Controlling the Translocation of Proteins through Nanopores with Bioinspired Fluid Walls

Erik C. Yusko, Jay M. Johnson, Sheereen Majd, Panchika Prangkio, Ryan C. Rollings, Jiali Li, Jerry Yang\*, Michael Mayer\*

\*Corresponding author: Michael Mayer, [mimayer@umich.edu](mailto:mimayer@umich.edu); Jerry Yang, [jerryyang@ucsd.edu](mailto:jerryyang@ucsd.edu)

## Table of Contents

Section S1. Electrical Resistance of Electrolyte-Filled Nanopores as a Function of Bilayer Thickness .....	3
S1.1 Model of Electrical Resistance in Electrolyte-Filled Nanopores .....	3
S1.2 Dimensions of Nanopores.....	4
S1.3 Dimensions of Nanopores after the Formation of a Lipid Bilayer Coating .....	7
S1.4 Thermal Actuation of the Diameter of Bilayer-Coated Nanopores.....	8
Section S2. Formation of Fluid Lipid Bilayers on the Silicon Nitride Substrate and Determination of Lateral Diffusion Constants.....	10
Section S3. Additional Evidence for a Bilayer Coating on the Walls of the Nanopores.....	14
S3.1 Bilayer Coatings Prevented Physisorption of Fluorescently-Labeled Streptavidin .....	14
S3.2 Analysis of the Electrical Current Noise Provides Additional Evidence for the Formation of a Bilayer inside the Pore.....	17
Section S4. Precise Control of the Surface Chemistry .....	19
Section S5. Evidence for the Binding of Proteins to Lipid-Anchored Ligands in the Bilayer and for the Translocation of Lipid-Bound Proteins through Bilayer-Coated Nanopores.....	21
S5.1 Control Experiments with Streptavidin .....	22
S5.2 Excess Free Biotin in Solution Abolished Resistive Pulses due to Anti-Biotin mAb.....	24
S5.3 Resistive-pulses in the Absence of Biotinylated Lipids could not be Time-Resolved.....	26
S5.4 Comparison of Diffusion Coefficients of Lipids and Diffusion Coefficients of Proteins in the Nanopore.....	30

Section S6. Translocations of Non-Spherical Proteins Generate Broad Distributions of  $\Delta I$ ..... 32

Section S7. Determining the Most Probable Value of  $t_d$  and its Error ..... 38

    S7.1 Determining the Most Probable  $t_d$  Value and its Error by Fitting Cumulative Distributions of  $t_d$  Values..... 38

    S7.2 Determining the Most Probable  $t_d$  Value by Fitting Histograms of  $t_d$  Values..... 40

Section S8. Calculating the Charge of Proteins from the Translocation Time of Lipid-Anchored Proteins ..... 42

    S8.1 Derivation of equation (3) in the main text ..... 42

    S8.2 Capillary Electrophoresis for Determining the Net Charge of Proteins ..... 45

    S8.3 Fitting Individual Distributions of  $t_d$  with both  $z$  and  $D$  as Fitting Parameters ..... 49

Section S9. Data Acquisition and Analysis of Resistive Pulses for Protein Detection ..... 51

Section S10. Preparation of Amyloid-Beta Samples and Gel-Electrophoresis ..... 54

## Section S1. Electrical Resistance of Electrolyte-Filled Nanopores as a Function of Bilayer Thickness

### S1.1 Model of Electrical Resistance in Electrolyte-Filled Nanopores

We explored the simplest possible model for the relationship between the electrical resistance and the geometry of the nanopore. Based on previous work, this model assumes that the smallest constriction of a nanopore and the resistivity of the electrolyte solution in the nanopore determine the total resistance, while the electrical resistance through the bulk electrolyte solution from the electrodes to the chip with the nanopore is negligible<sup>1,2</sup>. In the work presented here, the cylindrical nanopore and channel leading to the pore were the narrowest constrictions (Fig. S1).

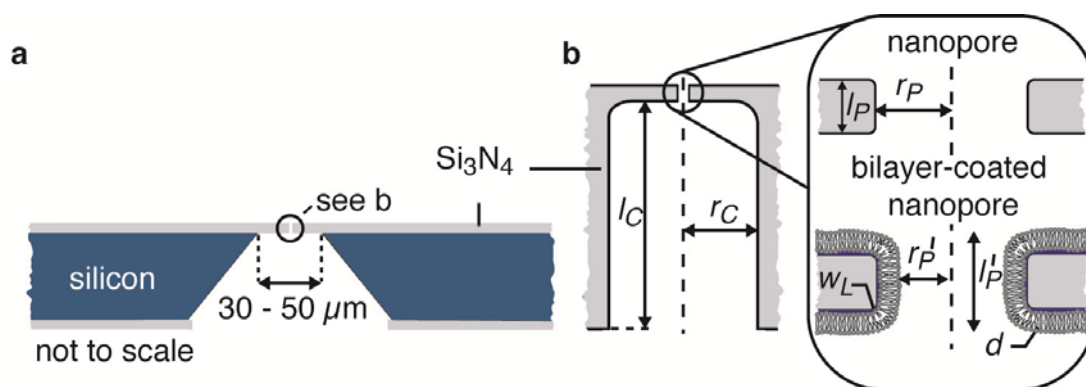


**Figure S1 | Schematic cross-section of the silicon chip and of the nanopore with the channel leading to the pore.**

**a**, Silicon chip (blue) with a silicon nitride layer (grey) on the top; the free-standing part of this  $\text{Si}_3\text{N}_4$  layer constitutes a window with a nanopore and with a channel through the silicon nitride that leads to the pore. **b**, Schematic illustration of this channel with a length  $l_C$  of  $258 \pm 9$  nm and a radius  $r_C$  of  $50 \pm 7.5$  nm, which led to a nanopore with radii  $r_P$  of 16 – 50 nm and lengths  $l_P$  of 12 – 22 nm, depending on the chip. Schematic illustration of a lipid bilayer coating with a thickness  $d$  and a water layer between the bilayer and the chip with a thickness  $w_L$ ; this bilayer coating increases the effective length of the nanopore to  $l_P' = l_P + 2(w_L + d)$  and reduces the effective radius to  $r_P' = r_P - w_L - d$ .

We described the nanopore, and the channel leading to the nanopore, as cylinders, each with a radius  $r$  (m) and length  $l$  (m) that were filled with an electrolyte with resistivity,  $\rho$  ( $\Omega \times \text{m}$ ). Due to the nanoscale diameter of the pore, the electric field lines converge from the bulk solution to the entrance of the nanopore, resulting in an additional resistive component called the access resistance,  $R_A$ <sup>3</sup>. Equation (S1) quantifies  $R_A$  for *one entrance* to a nanopore<sup>3</sup>.

$$R_A = \frac{\rho}{4r} \tag{S1}$$

Thus, the total resistance is a function of the resistance of the nanopore,  $R_P$ , the access resistance at each side of the pore,  $R_{AP}$ , the resistance due to the channel,  $R_C$ , and the access resistance from the bulk solution below the chip to the channel,  $R_{AC}$ . We treated these resistive components as resistors in series such that equations (S2) and (S3) describe the total resistance between two electrodes on opposite sides of a nanopore:

$$R = R_P + 2R_{AP} + R_C + R_{AC}, \tag{S2}$$

$$R = \frac{\rho l_P}{\pi r_P^2} + \frac{\rho}{2r_P} + \frac{\rho l_C}{\pi r_C^2} + \frac{\rho}{4r_C}, \tag{S3}$$

where  $l_P$  is the length of the nanopore,  $r_P$  is the radius of the nanopore,  $l_C$  is the length of the channel, and  $r_C$  is the radius of the channel (Fig. S1b).

### S1.2 Dimensions of Nanopores

We determined the radius of the nanopores,  $r_P$ , and of the channels leading to these pores,  $r_C$ , from transmission electron microscopy images (Fig. S2). To determine the total resistance of a pore for a given electrolyte, we measured the current through a pore at various applied voltages. For these measurements, we used an electrolyte solution containing 500 mM KCl and 10 mM

HEPES at pH 7.4 with a resistivity  $\rho$  of  $0.1517 \Omega \times \text{m}$  (measured with a calibrated conductance meter). Finally, we determined the length of the pore,  $l_P$ , by solving equation (S3) with the measured value of resistance  $R$ , the values of  $r_P$  and  $r_C$  determined from the TEM images, and

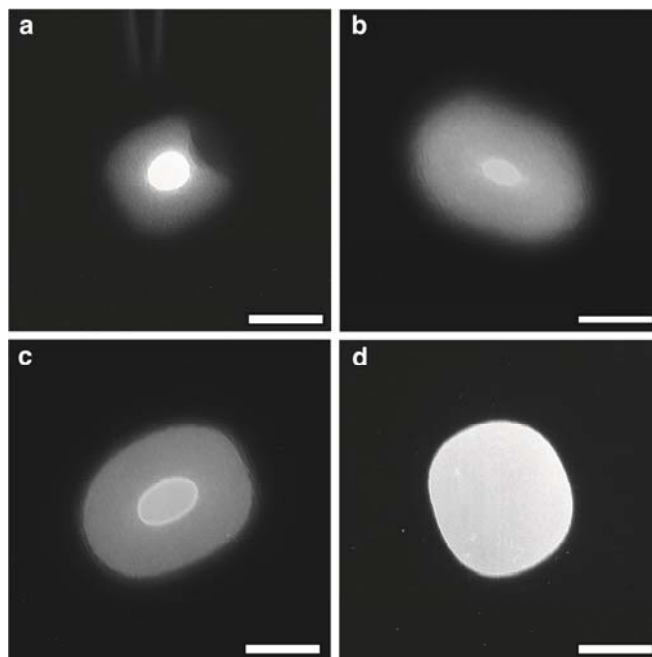


**Figure S2 | Transmission electron micrographs of several nanopores used in this work.** The brightest part in the center of each image depicts the shape and size of the nanopore and the surrounding circle with reduced brightness reflects the channel leading to the nanopore. All scale bars are 50 nm. **a**, Pore used for experiments with bilayers that contained lipids with different acyl-chain lengths ( $\langle r_P \rangle = 14$  nm,  $l_P = 12$  nm,  $r_C = 48$  nm, and  $l_C = 264$  nm). **b**, Pore used for sensing streptavidin ( $\langle r_P \rangle = 9.6$  nm,  $l_P = 18$  nm,  $\langle r_C \rangle = 49$  nm, and  $l_C = 258$  nm). **c**, Pore used for sensing monoclonal anti-biotin antibody and anti-biotin antibody Fab fragment ( $\langle r_P \rangle = 16.5$  nm,  $l_P = 22$  nm,  $\langle r_C \rangle = 53$  nm, and  $l_C = 255$  nm). **d**, Pore used for sensing aggregates of A $\beta$  peptides. For these experiments, the channel created by a focused ion beam without sculpting was used as the pore ( $\langle r_P \rangle = 48$  nm and  $l_P = 275$  nm;  $r_C = 0$  and  $l_C = 0$ ). Notation of a radius as  $\langle r \rangle$  indicates an area-equivalent radius calculated with equations (S4) or (S5). All dimensions refer to the pores before bilayer coating.

the known value for the thickness of the silicon nitride membrane ( $275 \pm 15 \text{ nm}^{4,5}$ ). Fig. S2 shows TEM micrographs of several pores used in this work; the caption lists the dimensions of these pores and specifies for which experiments they were used.

For cases in which the cross-section through the nanopore was ellipsoid rather than circular, we calculated an “area-equivalent” radius of the pore,  $\langle r_p \rangle$ , in such a way that the area of a perfect circle with radius  $r_p$  would be equal to the area of the ellipse with  $x$  corresponding to the major axis and  $y$  corresponding to the minor axis of the elliptical cross-section:

$$\langle r_p \rangle = \sqrt{xy} . \tag{S4}$$

Similarly, we calculated an area-equivalent radius for channels,  $\langle r_c \rangle$ , through the silicon nitride with an ellipsoid cross-section by:

$$\langle r_c \rangle = \sqrt{xy} . \tag{S5}$$

Table S1 lists the dimensions of nanopores used for experiments in the main text and the corresponding experiments.

**Table S1.** Dimensions of all nanopores used for experiments and corresponding experiment and figure. All dimensions refer to the pores before bilayer coating.

Figure	Description of experiment	Pore dimensions nm	Notes
1c	Resistance as a function of bilayer thickness	$r_p = 14; l_p = 12$	TEM image in Fig. S2a
1d	Resistance during a phase transition of DMPC lipids	$r_p = 13; l_p = 28$	-
2b, 3a, 4a	Sensing streptavidin	$\langle r_p \rangle = 9.6; l_p = 18$	TEM image in Fig. S2b
3b, 3c, 4b, 4c,	Sensing anti-biotin Fab fragments and anti-biotin monoclonal antibodies (IgG)	$\langle r_p \rangle = 16.5; l_p = 22$	TEM image in Fig. S2c
5	Sensing streptavidin as a function of charge and pH	$r_p = 10.5; l_p = 18$	-
6	Sensing aggregated of amyloid-beta ( $A\beta$ ) peptides	$\langle r_p \rangle = 48; l_p = 275$	TEM image in Fig. S2d

### *S1.3 Dimensions of Nanopores after the Formation of a Lipid Bilayer Coating*

To determine the dimensions of a nanopore after forming a lipid bilayer coating, we used the cylindrical pore shown in Figure S2a and added parameters for the thickness of the lipid bilayer,  $d$ , and for the thickness of the water layer between the silicon nitride and the lipid bilayer,  $w_L$ , to equation (S3) to obtain equation (S6), which is the same as equation (1) in the main text:

$$R = \frac{\rho(l_P + 2d + 2w_L)}{\pi(r_P - d - w_L)^2} + \frac{\rho}{2(r_P - d - w_L)} + \frac{\rho(l_C + 2d + 2w_L)}{\pi(r_C - d - w_L)^2} + \frac{\rho}{4(r_C - d - w_L)}. \quad (\text{S6})$$

Equation (S6) implies that the lipid bilayer and water layer did not conduct ionic current through the nanopore. These two layers, hence, reduced the effective radius of the nanopore by  $(d + w_L)$  and increased the effective length of the pore by  $2 \times (d + w_L)$  (Fig. S1b).

Note that we measured currents over tens of seconds in order to determine the resistance of the nanopore,  $R$ . As a result, fluctuations in the water layer or in the thickness of the supported lipid bilayer due to possible membrane undulations were averaged. We attribute the excellent agreement between the resistance of the nanopore and the thickness of the lipid bilayers (shown in Fig. 2c of the main text) to the use of the same chip and lipids with the same chemical head group (phosphatidylcholine) in these experiments. These conditions resulted in similar interactions between the bilayer, substrate, and water. In addition, we used the same cleaning procedure, same methods of preparing liposomes, and same electrolyte in each experiment.

*S1.4 Thermal Actuation of the Diameter of Bilayer-Coated Nanopores*

To calculate the thickness of a lipid bilayer, and hence, the effective open radius of a nanopore as a consequence of a thermal phase transition of the lipids, we described the resistivity,  $\rho$ , of the electrolyte as a function of temperature with equation (S7)<sup>6</sup>:

$$\rho = \frac{6\pi\eta}{CN_A e^2 \left( \frac{1}{r_+} + \frac{1}{r_-} \right)}, \tag{S7}$$

where the viscosity of water,  $\eta$  (Pa  $\times$  s), as a function of the temperature,  $T$  (K), is given by<sup>7</sup>:

$$\eta = (2.414 \times 10^{-5} \text{ Pa} \cdot \text{s}) \times 10^{\left( \frac{247.8\text{K}}{T-140\text{K}} \right)}, \tag{S8}$$

and  $C$  (mol  $\times$  m<sup>-3</sup>) is the concentration of a monovalent salt,  $N_A$  is Avogadro's constant (mol<sup>-1</sup>),  $e$  (C) is the elementary charge of an electron,  $r_+$  (m) is the radius of the hydrated cation, and  $r_-$  (m) is the radius of the hydrated anion in the electrolyte. To validate this model, we measured the resistance of a nanopore without a bilayer coating as a function of temperature. We used an electrolyte containing 500 mM KCl and controlled the temperature of the device and electrolyte with a Peltier cooler (Warner Instruments, Hamden CT). Fig. S3 shows the measured resistance as a function of temperature (squares). Note that the green curve is not a fit to the data; instead it reflects the calculated resistance as a function of temperature based on equations (S3), (S7) and (S8). In equation (S8), we used values for  $r_+$  of  $133 \times 10^{-12}$  (m) for K<sup>+</sup> ions and for  $r_-$  of  $181 \times 10^{-12}$  (m) for Cl<sup>-</sup> ions<sup>3</sup>.

To change the diameter of the nanopore, we coated the pore with a lipid bilayer of DMPC lipids (both acyl chains of DMPC are saturated and contain 14 carbons) and varied the temperature while measuring the resistance (Fig. S3, circles). We fit the data in Fig. S3 with equations (S6) – (S8) using the thickness of the bilayer,  $d$ , as the only fitting parameter. This fit



in the temperature range of 300 – 310 K returned the red curve ( $N = 5$ ,  $R^2 = 0.97$ ), and in the temperature range of 280 – 290 K, it returned the blue curve ( $N = 5$ ,  $R^2 = 0.95$ ) (Fig. S3). To calculate the change in  $d$  as a function of the thermal phase transition of the lipid bilayer, we used Maple™ 13 to solve equations (S6) – (S8) for  $d$ , with all parameters except temperature held constant (Fig. 2c in the main text). These calculations revealed a change in bilayer thickness,  $\Delta d$ , between the disordered liquid crystalline phase ( $T > 296$  K) and the ordered gel phase ( $T < 296$  K) of  $0.7 \pm 0.04$  nm (fit in Fig. 2c in the main text). This value of  $\Delta d$  is similar to reported values for  $\Delta d$  of DMPC bilayers of 0.9 - 1.1 nm<sup>8,9</sup>.

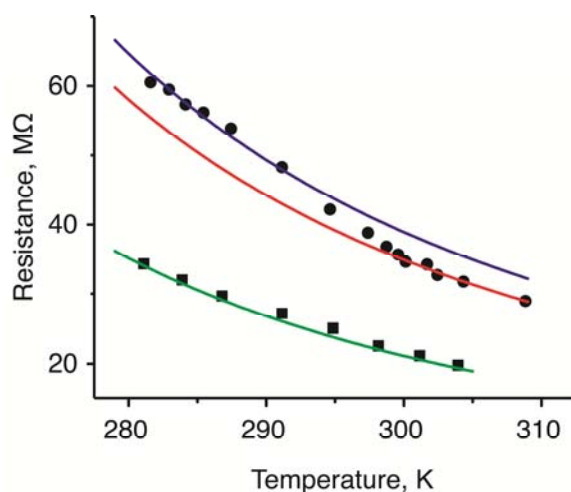


**Figure S3 | Shrinking and actuating the diameter of bilayer-coated nanopores with temperature.**

Resistance as a function of temperature in a nanopore coated with a bilayer of DMPC lipids, (●), and in a pore without a bilayer coating, (■). The green curve (—) represents a physical model based on equations (S3), (S7), and (S8) and described the resistance through the uncoated nanopore. Inclusion of the bilayer thickness,  $d$ , as a fitting parameter by employing equations (S6) – (S8) described the resistance through a bilayer coated-nanopore in the temperature range from 280 K to 290 K (—,  $R^2 = 0.95$ ,  $N = 5$ ) and in the temperature range from 300 K to 310 K (—,  $R^2 = 0.97$ ,  $N = 5$ ). The dimensions of the nanopore before bilayer formation were  $r_P = 13$  nm,  $l_P = 28$  nm,  $r_C = 50$  nm, and  $l_C = 247$  nm. The recording buffer contained 500 mM KCl and 10 mM HEPES (pH  $7.4 \pm 0.1$ ), and the applied potential difference was  $\pm 0.1$  V.

## Section S2. Formation of Fluid Lipid Bilayers on the Silicon Nitride Substrate and Determination of Lateral Diffusion Constants

Reimhult *et al.* demonstrated that liposome fusion on a silicon nitride surface forms a single supported lipid bilayer<sup>10</sup>. To prepare small unilamellar vesicles (SUVs), we dissolved the desired lipids in 100  $\mu\text{L}$  chloroform to a lipid concentration of 10 mM. We evaporated the solvent under vacuum using a rotary evaporator to form a lipid film in a round bottom glass flask with a volume of 10 mL. We resuspended this lipid film in an aqueous solution containing 150 mM KCl and 10 mM HEPES at pH 7.5 such that the lipid concentration was 2 mM. Finally, we formed SUVs via tip sonication (Branson Sonifier 150) of the solution with a power of 3 – 4 W for  $\sim 10$  min and stored these solutions at 4  $^{\circ}\text{C}$  for up to 4 days. We formed the supported lipid bilayer on the chips as described in the Methods Section of the main text.

We used epifluorescence microscopy to confirm the formation of a fluid lipid bilayer for experiments with bilayer-coated nanopores. To visualize the lipid bilayer, we prepared all liposomes with 0.8 mol% of lipids labeled with the fluorophore rhodamine B (1,2-dipalmitoyl-*sn*-glycero-3-phosphoethanolamine-N-(lissamine rhodamine B sulfonyl)) (Rh-PE, Avanti Polar Lipids). To form the lipid bilayer, we incubated the top side of the chip in a solution containing Rh-PE labeled liposomes for 5 – 10 min followed by rinsing with pure water for 5 – 10 min. We used a Nikon E600FN upright microscope equipped with an Evolution MP (Media Cybernetics, Canada) camera and a 60 $\times$  water-dipping objective (NA = 1.00) to image the bilayers. Fig. S4a shows a fluorescent micrograph (false-colored in red) that confirmed the presence of a supported lipid bilayer on the silicon nitride substrate. The sharply defined square in the middle of the image is the free-standing silicon nitride membrane. A line scan across the silicon nitride membrane (solid white line) quantified the fluorescence intensity as a function of the position along this line (Fig. S4a). Interestingly, we observed four values of fluorescence intensity along

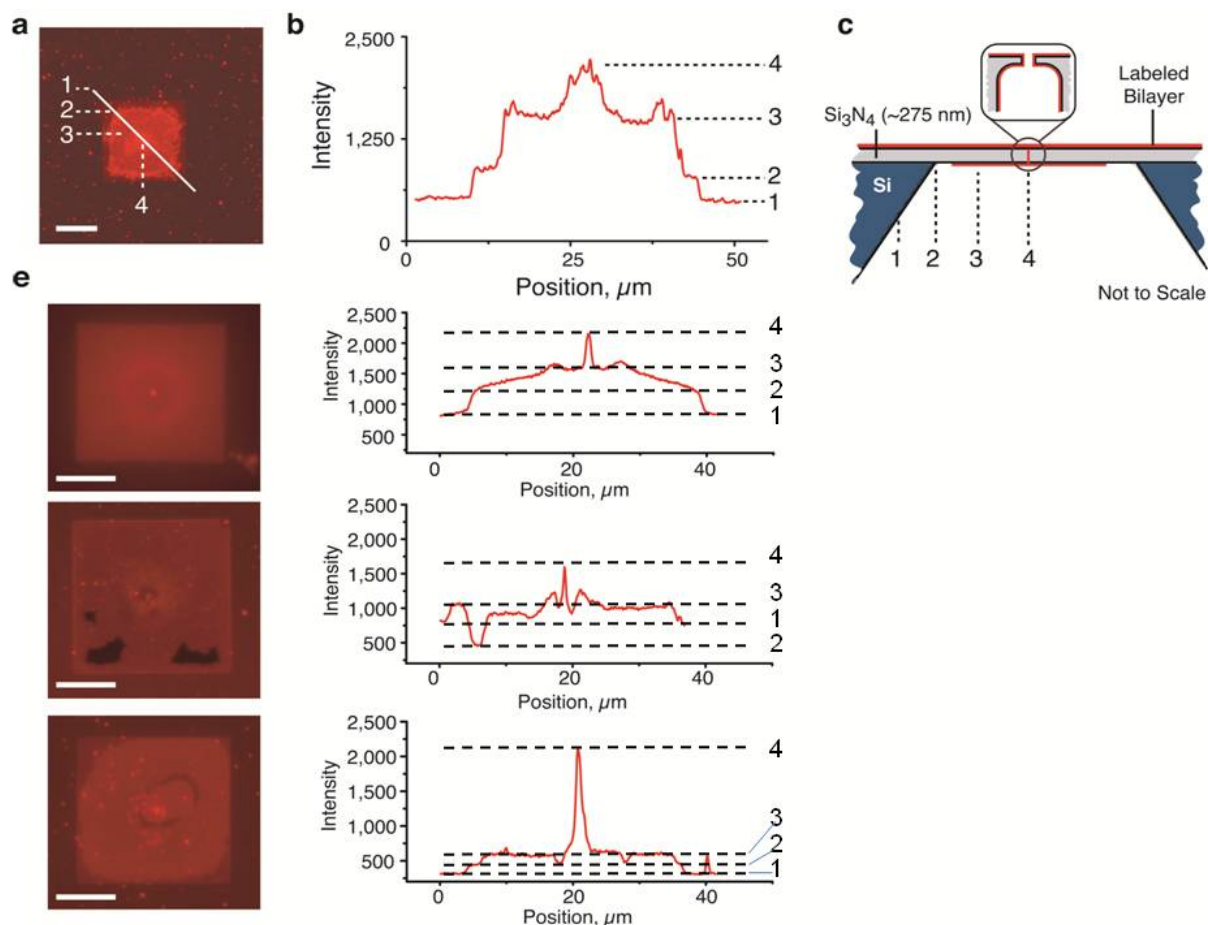


**Figure S4 | Fluorescence micrographs of Si-Si<sub>3</sub>N<sub>4</sub> chips with a supported lipid bilayer containing Rh-PE lipids and corresponding line scans. a**, Epifluorescence micrograph with a line scan to quantify the fluorescence intensity along the path shown by the solid white line. This pore had an area-equivalent diameter of 33.5 nm and a length of 22 nm without the bilayer coating. **b**, Plot of fluorescence intensity as a function of position along the line scan. The numbers 1-4 correspond to the numbers in **a** to the location on the chip indicated in the schematic illustration **c**. **e**, Additional epifluorescence micrographs showing the diffraction limited spot at the location of the nanopore. Line scans were measured from the opposite corners of the silicon nitride window similar to that in panel **a**. From top to bottom these pores had area-equivalent diameters of 31 nm, 33.5 nm, and 20 nm; and lengths of 20 nm, 22 nm, and 18 nm. All bilayers were labeled with 0.8 mol% Rh-PE. All scale bars correspond to 10  $\mu$ m.

this path. The lowest intensity occurred in area 1 ( $I = 528 \pm 15$ ); a location in which the bulk silicon chip supported the silicon nitride membrane. Moving along the line scan to an area over part of the free-standing silicon nitride membrane, indicated as area 2, we observed a slightly greater intensity ( $I = 873 \pm 31$ ) than in area 1. We attribute the reduced intensity in area 1 compared to area 2 to destructive interference from light reflected by the bulk silicon chip below area 1<sup>11</sup>. Moving further along the line scan toward the center of the free-standing, silicon nitride membrane (area 3), we observed a fluorescence intensity approximately twice the intensity ( $I = 1,542 \pm 29$ ) of area 2. This result indicates that area 3 contained approximately twice the amount of fluorescent Rh-PE lipids than area 2 and is consistent with a supported bilayer on both sides of the free-standing, silicon nitride membrane. Finally, area 4, in the center of the free-standing, silicon nitride membrane and at the location of the nanopore, had the greatest fluorescence intensity ( $I = 2,222$ ). We attribute this high intensity to the presence of a lipid bilayer on the vertical walls of the nanopore and channel (see Fig. S1), and hence, to an increased number of Rh-PE lipids in the optical path. Fig. S4e shows three additional fluorescence micrographs with a spot of high intensity in the center of the free standing, silicon nitride membrane at the precise location of the nanopores. The width of these spots at  $1/e^2$  of their maximum intensity,  $w_{(1/e^2)}$ , ranged from 0.8  $\mu\text{m}$  to 1.8  $\mu\text{m}$ . These values are 2-5 times larger than the theoretical diffraction-limited spot size of 0.33  $\mu\text{m}$  that we calculated for this objective with equation (9)<sup>12</sup>:

$$w_{(1/e^2)} = \frac{2\lambda}{n\pi NA}, \quad (9)$$

where,  $\lambda$  is the wavelength of light (here  $\sim 700$  nm),  $n$  is the index of refraction of the medium (here 1.33), and NA is the numerical aperture of the objective (here 1.00). The larger than

expected values for the size of the diffraction-limited spot could be due to reflection or refraction occurring at the interface between the aqueous solution and the transparent silicon nitride structure of the nanopore. Furthermore, equation (9) predicts the size of the smallest spot that can be obtained theoretically given all of the optics were perfect – real microscopes typically cannot reach this theoretical limit. Regardless of deviations from the theoretically expected spot size, the images in Fig. S4e confirm the observations in Fig. S4a, b with regard to the fluorescence intensity from bilayers on the chips. These results, in combination with the well-defined shrinkage of the pore diameter by bilayer coatings of various lipids (Fig. 2b in the main text) and the results from Fig. 3 and 4 in the main text, suggest that a supported lipid bilayer formed on the silicon nitride, on the inner walls of the nanopore and channel, and on the underside of the free-standing, silicon nitride membrane.

To confirm the fluidity of the supported lipid bilayers and to determine lateral diffusion constants of the lipids, we performed fluorescence recovery after photobleaching (FRAP) experiments (Fig. S4a and b) on the bilayer at a location outside, but near, the free-standing, silicon nitride membrane (*i.e.*, in area 1 of Fig. S4a)<sup>13</sup>. We analyzed these images by calculating the difference between the mean fluorescence intensity of the photobleached spot and a second spot on the same bilayer that was not photobleached. We normalized to the maximum difference between these two intensities and determined the diffusion coefficients by the equation,  $D_L$  ( $\text{nm}^2 \times \mu\text{s}^{-1}$ ) =  $0.224 \times \omega^2$  ( $\text{nm}$ )<sup>2</sup> /  $t_{1/2}$  ( $\mu\text{s}$ ), where  $\omega$  is the radius of the bleached spot and  $t_{1/2}$  is the half time of the fluorescence recovery<sup>14,15</sup>. We obtained the value of  $t_{1/2}$  from an exponential curve fit through the data (Fig. S5b). On the chip used in Fig. S5 and shown in Fig. S2b, the diffusion coefficient for bilayers containing POPC lipids was  $1.13 \pm 0.13 \text{ nm}^2 \times \mu\text{s}^{-1}$  and for bilayers containing DAPPC lipids it was  $1.56 \pm 0.16 \text{ nm}^2 \times \mu\text{s}^{-1}$ . These values are close to reported values

of diffusion coefficients of supported bilayers, which range from  $2 \text{ nm}^2 \times \mu\text{s}^{-1}$  to  $5 \text{ nm}^2 \times \mu\text{s}^{-1}$  and are typically obtained on glass or  $\text{SiO}_2$  surfaces instead of  $\text{Si}_3\text{N}_4$  surfaces<sup>16,17</sup>.

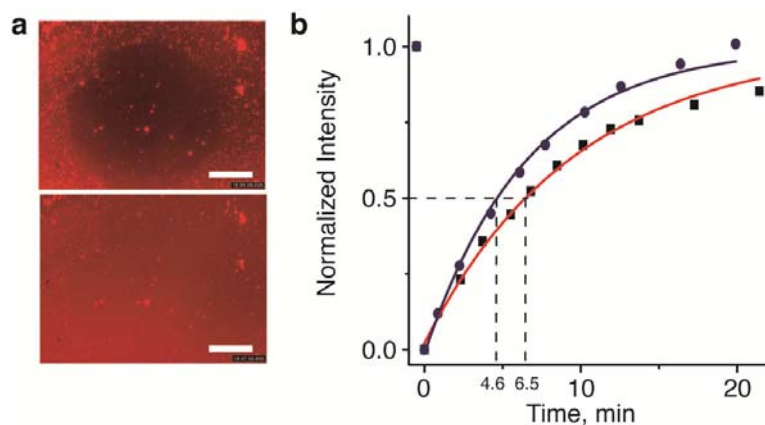


**Figure S5 | Fluorescence micrographs for determining bilayer fluidity by fluorescence recovery after photobleaching (FRAP) experiments.** **a**, Epifluorescence micrographs indicating the recovery of fluorescence in a photobleached spot of the lipid bilayer on the Si-Si<sub>3</sub>N<sub>4</sub> chip. **b**, Plot of intensity versus time from two separate FRAP experiments on a chip that was coated with a bilayer containing 98.8 mol% POPC (■) or with 98.8 mol% DΔPPC (●). The larger  $t_{1/2}$  value for POPC lipids compared to DΔPPC lipids indicated the increased viscosity of POPC bilayers compared to DΔPPC bilayers. All bilayers were labeled with 0.8 mol% Rh-PE and contained 0.4 mol% of 1,2-dipalmitoyl-*sn*-glycero-3-phosphoethanolamine-N-(cap biotinyl) (biotin-PE) because the same chips were later used to sense the translocation of streptavidin (Fig. 3a and 4a in the main text). Images in **a** were both contrast enhanced to the same extent to increase clarity. The scale bars correspond to 25  $\mu\text{m}$ .

### Section S3. Additional Evidence for a Bilayer Coating on the Walls of the Nanopores

#### S3.1 Bilayer Coatings Prevented Physisorption of Fluorescently-Labeled Streptavidin

To provide additional evidence that a supported lipid bilayer formed on the walls inside the nanopores, we incubated a chip containing a nanopore with rhodamine-labeled streptavidin (SA-TRITC). We incubated the same piranha-cleaned chip with SA-TRITC in one experiment

*after* forming a supported lipid bilayer on the chip (and in the pore) and in the other experiment *before* forming the bilayer. Figure S6a shows that in the absence of a bilayer coating, SA-TRITC physisorbed to the silicon nitride surface including in the center of the silicon nitride window where a bright spot of fluorescence indicates that SA-TRITC also physisorbed onto the walls inside the uncoated nanopore. Similar to the line scans shown in Fig. S4, the width of the diffusion limited high intensity spot in Fig. S6a was 0.9  $\mu\text{m}$ . In contrast, Fig. S6b shows that the same chip, after being cleaned and subsequently coated with a lipid bilayer, did not physisorb a detectable amount of rhodamine-labeled streptavidin. Additionally, at the center of the silicon nitride window and the location of the nanopore, we did not detect an increase in the intensity of fluorescence. This result suggests that the vertical walls inside the nanopore were also coated with a lipid bilayer that prevented the physisorption of SA-TRITC.

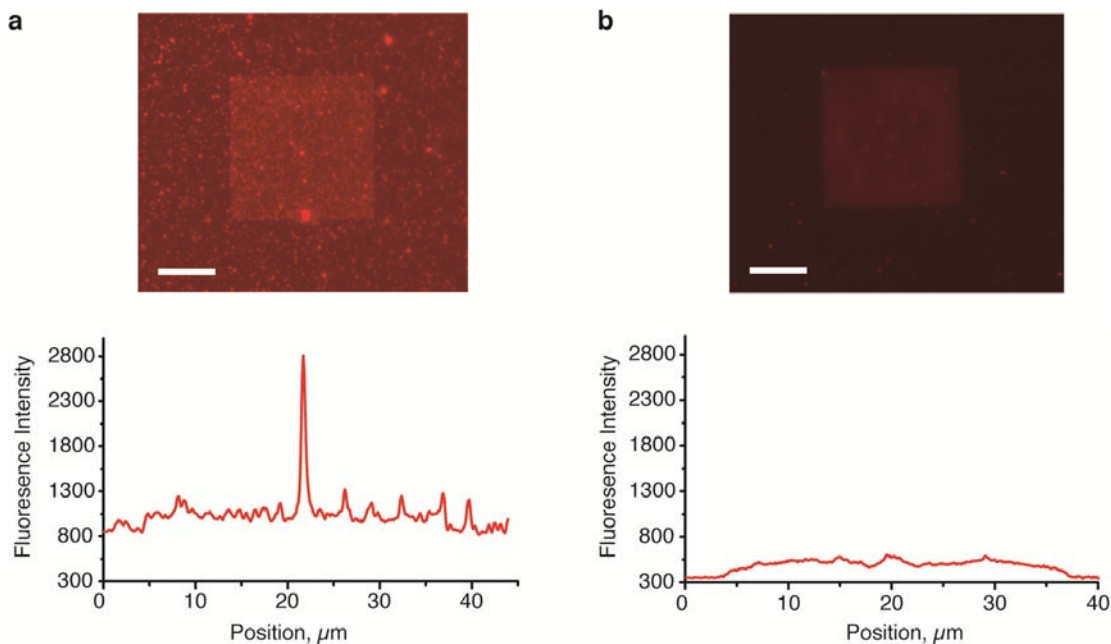


**Figure S6 | Fluorescence micrographs of silicon-nitride windows with a nanopore after exposure to fluorescently labeled-streptavidin. a,** Fluorescence micrograph taken of the silicon nitride window after physisorption of streptavidin-TRITC onto a chip that was cleaned with a fresh 3:1 mixture of concentrated sulfuric acid and a 30% (v/v) hydrogen peroxide solution (Piranha solution). The line scan beneath the image corresponds to the intensity of fluorescence along a diagonal path across the silicon nitride window through the location of the nanopore at its center. **b,** Fluorescence micrograph taken of the same silicon nitride window but after formation of a supported lipid bilayer of POPC lipids followed by incubation with streptavidin-TRITC. The line scan beneath the image corresponds to the intensity of fluorescence along a diagonal path across the silicon nitride window through the location of the nanopore at its center. The nanopore for these experiments had an area-equivalent diameter of 110 nm and a length of 275 nm. Scale bars correspond to 10  $\mu\text{m}$ . The same camera and exposure settings were used to acquire both images.



### *S3.2 Analysis of the Electrical Current Noise Provides Additional Evidence for the Formation of a Bilayer inside the Pore*

Since supported lipid bilayers are fluid sheets, lipid molecules within the bilayer are in dynamic motion. In addition, the water layer between the lipid bilayer and the silicon nitride substrate fluctuates around an average value. We hypothesized that the resulting bilayer undulations may influence the electrical noise in current recordings. Figure S7a, b compare the power spectra of the noise as a function of frequency for two chips with nanopores before and after generating a supported lipid bilayer. As expected, when the pore was coated with a fluid lipid bilayer, the noise increased at low frequencies ( $< 2$  kHz) compared to the uncoated pore. Since this increased noise was likely due to dynamic motions consistent with a supported lipid bilayer inside the nanopores, it provides additional evidence for the formation of a lipid bilayer on the walls inside the nanopores. To test this hypothesis, we obtained power spectra of the noise with a chip that contained a very small nanopore with area-equivalent diameter of 9 nm. The diameter of this nanopore was too small for a supported lipid bilayer to form on the interior walls of the pore. In this case, spreading of fluorescently-labeled liposomes on the top side of the chip coated only this top side while no increased fluorescence could be detected at the location of the pore and no doubled fluorescence intensity could be detected from creeping of fluorescent bilayers through the pore to the other side of the silicon nitride window. Figure S7c, d shows that in this case, the electrical noise in the system remained relatively unchanged compared to the nanopores with a diameter large enough to accommodate a bilayer coating inside the pore. In both experiments, we confirmed by FRAP experiments that the bilayer near the pore was fluid. Together these results provide additional evidence for the formation of a fluid lipid bilayer on the walls inside the nanopore.

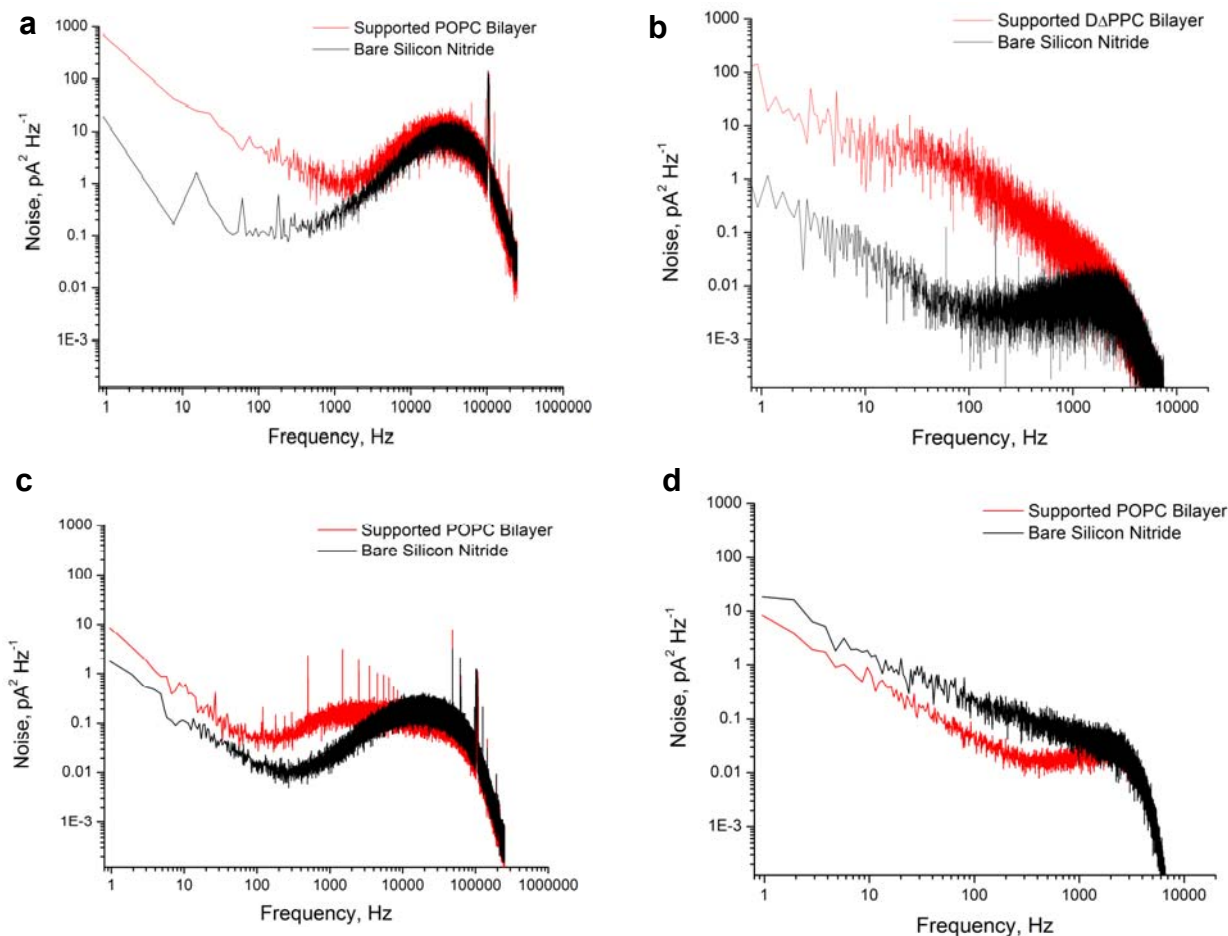


**Figure S7 | Power spectra of the electrical current noise from chips with a bilayer coating and from chips without a bilayer coating. a, b,** Power spectra of the noise before and after formation of supported lipid bilayers from two different lipids on the same chip while a voltage of -0.1 V was applied. The nanopore had a diameter of 28 nm before formation of the supported lipid bilayer (a, POPC lipids; b, DΔPPC lipids). In b, the current recording was recorded with the hardware filter of the amplifier set to a cut-off frequency of 2 kHz. c, d, Power spectra of the noise from two independent experiments with a chip containing a very small area-equivalent diameter of 9 nm, which was too small for the formation of a lipid bilayer inside the nanopore. In d, the current recording was recorded with the hardware filter of the amplifier set to a cut-off frequency of 2 kHz. The electrolyte for all recordings contained 500 mM KCl and 10 mM HEPES with a pH of  $7.4 \pm 0.1$ .

## Section S4. Precise Control of the Surface Chemistry

The surface chemistry of bilayer-coated nanopores can be precisely controlled by the nature of the polar head groups of the lipids used in the bilayer coating. To demonstrate this capability, we formed several liposome preparations from POPC lipids that contained different mole fractions of 1,2-dioleoyl-*sn*-glycero-3-phosphate (DOPA), a lipid with a negatively charged head group. After vesicle fusion of these liposomes onto Si/Si<sub>3</sub>N<sub>4</sub> chips with a nanopore to generate the bilayer coating, we measured the electrical resistance through the nanopore. Since under conditions of low ionic strength, positively charged ions accumulate near the surface of a negatively charged bilayer, we expected to observe a decrease in the resistance of the pore with increasing mole fractions of DOPA.<sup>18</sup> Fig S8 confirms that the resistance of the bilayer coated nanopore decreased with increasing mole fractions of DOPA lipids inside the nanopore walls.

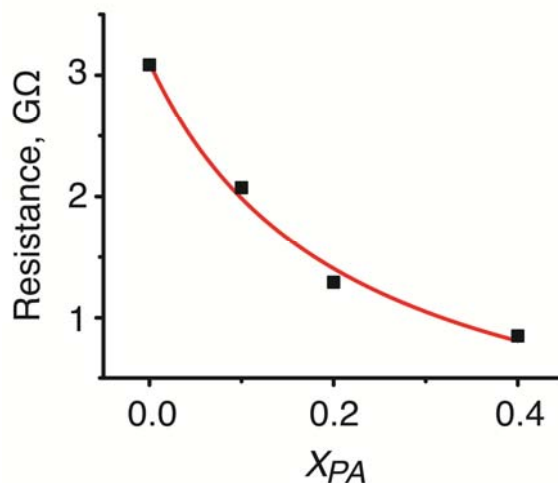


**Figure S8 | Nanopore coatings with increasing mole fractions of negatively charged lipids reduce the resistance of the nanopore in electrolytes with low ionic strength.** The supported lipid bilayers were formed from liposomes with the indicated mole fractions,  $X_{PA}$ , of DOPA lipids with a background of POPC lipids. The pore used for these experiments had a diameter of 28 nm before the bilayer coating. The electrolyte had an ionic strength of ~2.5 mM and contained 750  $\mu$ M CaCl<sub>2</sub> and 250  $\mu$ M KCl with a pH of ~ 7.

To demonstrate that this decrease in the resistance was a nanoscopic effect, as predicted by the Gouy-Chapman theory, we compared the resistance of a conical pore (tip diameter 500 nm) whose walls were coated by an electrically neutral bilayer (~99 mol% POPC) to the resistance of the same pore with a negatively charged bilayer coating (~40 mol% DOPA and ~59 mol% POPC). Using the same electrolyte as in Fig. S8, the resistance of this large pore remained independent of the presence of a neutral or negatively charged bilayer coating (Fig. S9). This result confirms that the observations in Fig. S8 were due to nanoscopic phenomena in pores with diameters that are significantly smaller than 500 nm; it also provides additional evidence for the formation of a negatively charged bilayer on the walls inside the nanopore.

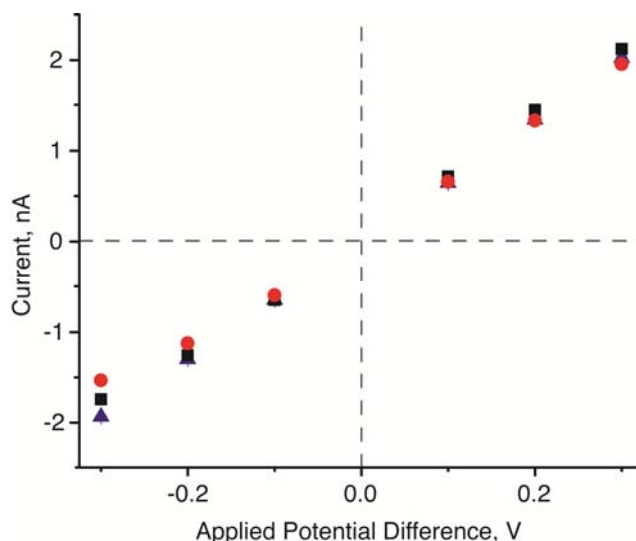


**Figure S9 | Charges on the surface of a pore with a diameter of 0.5  $\mu\text{m}$  did not significantly affect the permeation of ions, and hence resistance, through the pore.** Currents were measured as a function of applied potential difference through a conical pore (tip diameter 500 nm) without a bilayer (■), through the same pore with an electrically neutral bilayer coating of POPC lipids (▲), and through the same pore with a bilayer coating containing 40 mol% of negatively charged lipids (●). The recording electrolyte was the same as in Fig. S8.

## Section S5. Evidence for the Binding of Proteins to Lipid-Anchored Ligands in the Bilayer and for the Translocation of Lipid-Bound Proteins through Bilayer-Coated Nanopores

We used the amplitude of resistive pulses,  $\Delta I$ , to distinguish the translocation of streptavidin (SA), monoclonal anti-biotin antibody (mAb), and anti-biotin Fab fragments (Fab) through nanopores. These pores were coated with a bilayer that contained biotinylated lipids (biotin-PE) at the specified mole fractions. To confirm that resistive pulses were due to proteins that were bound to biotin-PE, we performed several control experiments that entailed: 1) replacing the electrolyte in the top compartment with a solution that did not contain SA to investigate if the frequency of events would be reduced (as expected for unbound SA) or remain the same (as expected for lipid-anchored SA); 2) presenting an excess of soluble biotin in solution in the presence of mAb on a chip that contained a bilayer-coated nanopore with biotin-PE lipids; and 3) detecting the translocation of SA, mAb, and Fab with bilayer-coated nanopores that did not contain biotin-PE lipids. We describe these experiments in detail in the following paragraphs, but briefly, when the protein could bind to biotin-PE in the bilayer coating, we observed 20-500 times more frequent translocation events than under conditions in which the protein could not bind to biotin-PE. Furthermore, we observed significantly prolonged translocation times when proteins could bind to biotin-PE; these increased  $t_d$  values permitted time-resolved measurements of  $\Delta I$  (and therefore quantitative estimation of protein volume). Finally, the viscosity of the bilayer coating influenced the translocation time of proteins passing through the nanopore only when proteins could bind to biotin-PE. We show that the diffusion coefficients of the proteins in the nanopore under these conditions were similar to the diffusion coefficients of the lipids in the bilayer coating, and we present a simple model for predicting the translocation times for proteins through a nanopore. We conclude from these results that bilayer-coated nanopores with biotin-PE lipids detected specifically proteins that bound to these lipid

anchored biotin groups. Moreover, resistive pulses were due to the translocation of protein-(biotin-PE) complexes through the nanopore because biotin-PE remained mobile within the fluid bilayer coating of the nanopore. The unique ability of bilayer-coated nanopores to exploit the viscosity of a fluid bilayer coating in order to reduce the translocation speed of proteins made it possible to determine the volume of proteins accurately and, consequently, to distinguish anti-biotin Fab fragments from anti-biotin mAbs.

### *S5.1 Control Experiments with Streptavidin*

We hypothesized that SA would remain bound to biotin-PE for extended periods of time due to the very slow off-rate of the SA to biotin interaction ( $k_{off} \sim 10^{-6} \text{ s}^{-1}$ )<sup>19</sup>. Consequently, after washing the liquid compartments to remove unbound SA from solution, we expected to observe a continuation of frequent resistive pulses with a nanopore coated with a bilayer containing biotin-PE. To start this experiment, we generated a bilayer-coated nanopore that contained 0.15 mol% biotin-PE lipids. After adding 6 pM SA to the electrolyte on top of the fluidic setup, we applied a voltage of -0.1 V and observed resistive pulses at a frequency of  $\sim 45 \text{ s}^{-1}$  (Fig. S10a). Consistent with resistive pulses due to proteins with a net negative charge, we observed a 28-fold decrease in the frequency of resistive pulses after changing the polarity of the applied voltage to +0.1 V (frequency of  $\sim 1.6 \text{ s}^{-1}$ ). After rinsing the fluidic channels periodically for 3 h, we again applied a voltage of -0.1 V and observed resistive pulses at a frequency similar to the frequency before washing ( $41 \text{ s}^{-1}$  versus  $45 \text{ s}^{-1}$ , Fig. S10a). When we repeated this experiment with a bilayer-coated nanopore that did not contain biotin-PE lipids, we observed almost no resistive pulses (frequency of  $\sim 0.09 \text{ s}^{-1}$ , Fig. 2b from the main text and Fig. S10a). Together these results confirm that the observed resistive pulses were due to translocation of SA bound to lipid-

anchored biotin through the nanopore while biotin-PE remained mobile within the fluid bilayer coating.

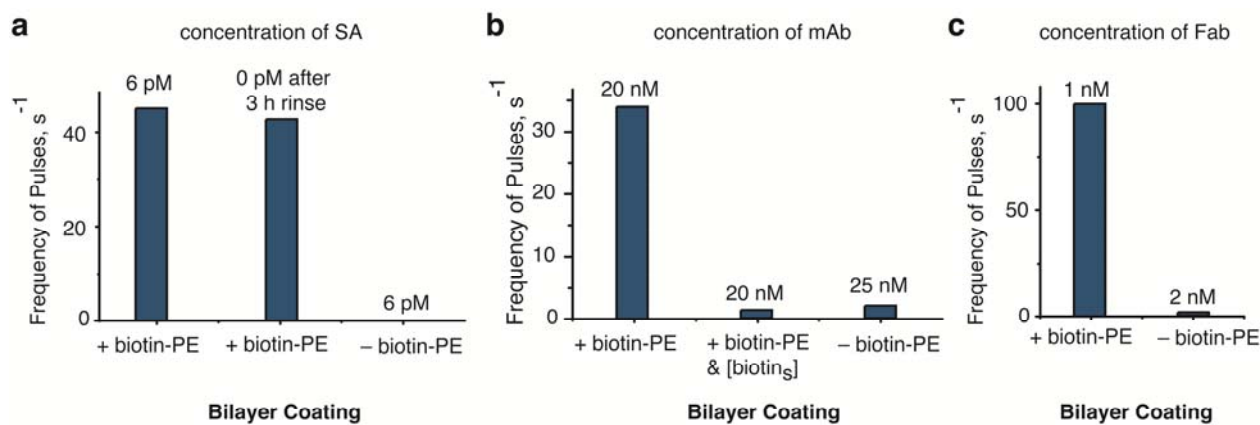


**Figure S10 | Bar graphs comparing the frequency of resistive pulses due to the translocation of streptavidin, anti-biotin mAb, and anti-biotin Fab fragments through bilayer-coated nanopores with biotin-PE lipids and respective control experiments.** **a**, Frequency of resistive pulses due to translocation of SA through a nanopore with a bilayer coating that contained biotin-PE lipids and after exchanging the electrolyte for 3 h to remove SA from solution compared to a coating without biotin-PE lipids (in this case the frequency of events was 0.09 s<sup>-1</sup> and is too low to be seen as a bar). **b**, Frequency of resistive pulses due to the translocation of anti-biotin mAb through a nanopore with a bilayer coating that contained biotin-PE lipids compared to the same experiment after adding 10 μM of soluble biotin to the solution and compared to an experiment with a nanopore coating that did not contain biotin-PE lipids. **c**, Frequency of resistive pulses due to the translocation of anti-biotin Fab through a nanopore with a bilayer coating that contained biotin-PE lipids compared to a coating without biotin-PE lipids. The concentrations of the proteins are shown above the bars. Bilayers were formed from ~99 mol% POPC, 0.8 mol% Rh-PE, and if indicated, 0.15 mol% biotin-PE.

### S5.2 Excess Free Biotin in Solution Abolished Resistive Pulses due to Anti-Biotin mAb

To provide additional evidence for the specificity of detection of proteins that were targeted by lipid-anchored biotin (*i.e.* streptavidin, anti-biotin mAb, or anti-biotin Fab fragments) with bilayer-coated nanopores, we performed a control experiment by adding a high concentration of soluble biotin (10  $\mu\text{M}$ ) to an ongoing experiment with a bilayer-coated nanopore that contained biotin-PE. We hypothesized that the excess biotin in solution would compete for biotin binding sites on these proteins, and consequently, the frequency of resistive pulses after the addition of biotin would decrease. To start this experiment, we coated a nanopore with a bilayer that contained biotin-PE lipids. After adding 20 nM anti-biotin mAb to the solution in the top fluid compartment, we observed resistive pulses at a frequency of 34  $\text{s}^{-1}$  (Fig. S10b and S11a). After adding 10  $\mu\text{M}$  soluble biotin to the solution, we observed significantly fewer resistive pulses (frequency of 1.3  $\text{s}^{-1}$ ) demonstrating that approximately 96% of the resistive pulses in Fig. S11a were due to mAb that was bound to biotin-PE (Fig. S10b and Fig. S11b). This result indicates that the detection of the proteins (*i.e.* streptavidin, mAb, or Fab) required binding of the proteins to biotin-PE lipids and that the proteins moved through the nanopore while bound to mobile biotin-PE lipids in the fluid, lipid bilayer coating.



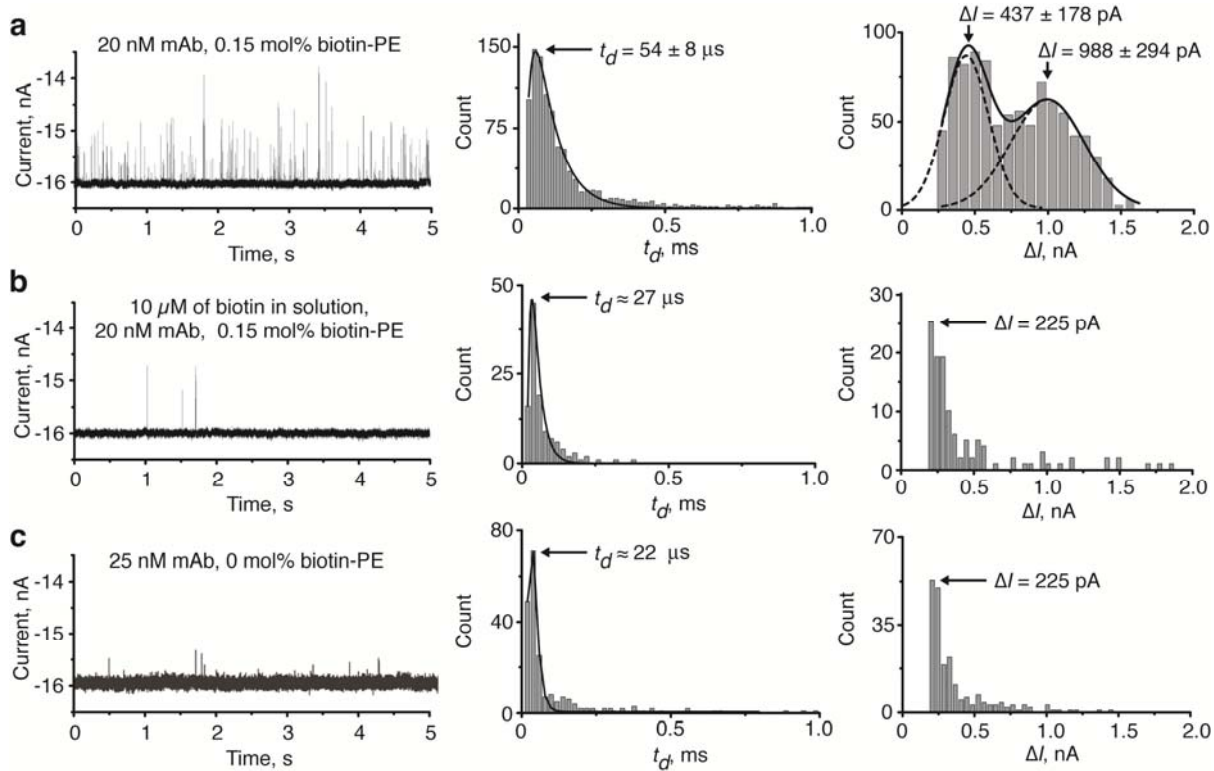


**Figure S11 | Detection of monoclonal anti-biotin IgG<sub>1</sub> antibody (mAb) with a bilayer-coated**

**nanopore.** **a**, Current versus time trace showing resistive pulses due to translocation of mAbs that were bound to biotin-PE lipids in the bilayer coating and analysis of  $t_d$  and  $\Delta I$  of the corresponding resistive pulses. Resistive pulses occurred at a frequency of  $34 \text{ s}^{-1}$ . **b**, Current versus time trace recorded after the addition of excess biotin ( $10 \mu\text{M}$ ) to the solution, illustrating the reduced frequency of resistive pulses ( $1.3 \text{ s}^{-1}$ ) and analysis of  $t_d$  and  $\Delta I$  of the corresponding resistive pulses. **c**, Current versus time trace recorded using the same nanopore as **a** and **b** but with a bilayer coating that did not contain biotin-PE lipids, illustrating the reduced frequency ( $2 \text{ s}^{-1}$ ) of resistive pulses even at a concentration of mAb of 25 nM and analysis of  $t_d$  and  $\Delta I$  of the corresponding resistive pulses. Distributions of  $t_d$  values were fit with equation (S10) as described in Supplementary Section S5.4 and S7.1. Bilayers were formed from  $\sim 99$  mol% POPC, 0.8 mol% Rh-PE, and if indicated, 0.15 mol% biotin-PE. The experiments were performed with the nanopore shown in Supplementary Fig. S2c. The recording buffer contained 2.0 M KCl and 10 mM HEPES buffered at a pH of  $7.4 \pm 0.1$ , and currents were recorded at an applied potential difference of  $-0.1 \text{ V}$ .

We hypothesized that in this control experiment, the excess biotin in solution would occupy the majority of the binding sites of anti-biotin mAb and would therefore prevent the mAb from binding to biotin-PE lipids. Consequently, we expected the translocation of mAb through the nanopore to occur faster than before the addition of excess biotin (*i.e.* when the mAb moved through the nanopore as a lipid-anchored mAb-biotin-PE complex). The histograms of  $t_d$  and  $\Delta I$  values in Fig. S11a and S11b confirmed this expectation by illustrating that the most frequently observed translocation time decreased from  $54 \pm 8 \mu\text{s}$  to  $\sim 27 \mu\text{s}$  after adding excess biotin in solution. This result indicates that the viscosity of the bilayer coating reduced the translocation speed (*i.e.* increased the value of  $t_d$ ) of mAbs that were bound to biotin-PE lipids in the bilayer by at least a factor of two compared to translocation of unbound mAbs. Furthermore, in contrast to the translocation times for mAb that was bound to biotin-PE ( $t_d = 54 \pm 8 \mu\text{s}$ ), translocation times for unbound mAb ( $t_d \approx 27 \mu\text{s}$ ) were shorter than the bandwidth of the recording setup (Supplementary Section S9), and consequently, the values for  $\Delta I$  were attenuated because they were not time resolved (Fig. S11b).

### S5.3 Resistive-pulses in the Absence of Biotinylated Lipids could not be Time-Resolved

To confirm that time-resolved detection of streptavidin, anti-biotin mAb, and anti-biotin Fab fragments with bilayer-coated nanopores required biotin-PE lipids in the bilayer coating, we generated bilayer-coated nanopores that did not contain biotin-PE and added SA, mAb, or Fab fragments. We analyzed the current recordings to determine the frequency of resistive pulses, the values of  $t_d$ , and the magnitudes of  $\Delta I$ . Figure S10 shows that bilayers without biotin-PE resulted in resistive pulses at 20-500-fold lower frequencies than bilayers with biotin-PE (see also Fig. S11 and S12a for original current traces). These results suggest that biotin-PE in the supported

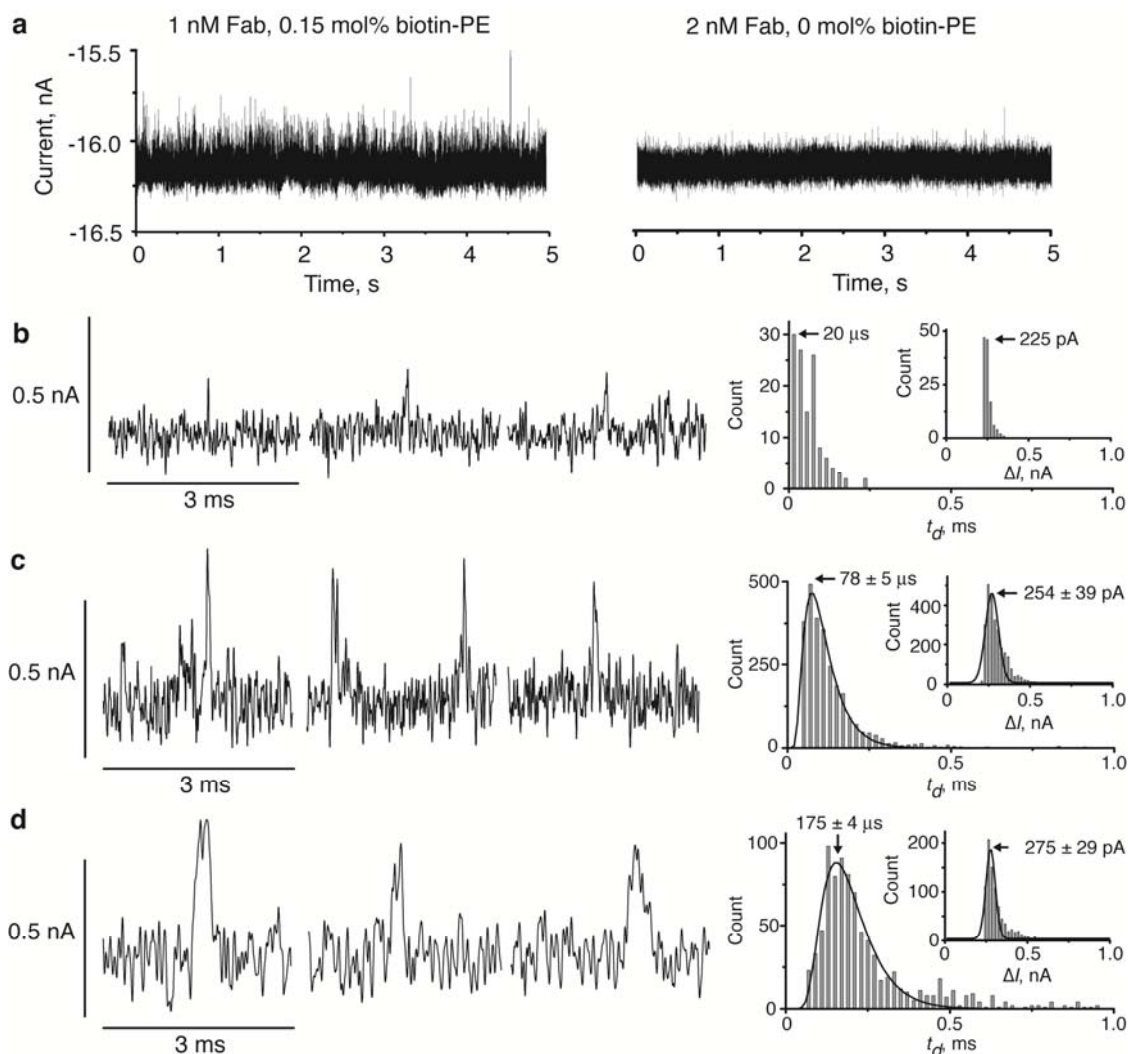


**Figure S12 | Viscosity of bilayers can slow the translocation of anti-biotin Fab fragments that are bound to biotin-PE lipids permitting time-resolved determination of the peak amplitude of resistive pulses.** **a**, Current traces showing resistive pulses due to the translocation of Fab fragments through the nanopore. Resistive pulses were observed at a frequency of  $\sim 100 \text{ s}^{-1}$  with bilayer coatings that contained biotin-PE, whereas bilayer coatings without biotin-PE resulted in resistive pulses at a frequency of  $2 \text{ s}^{-1}$ .

**b**, Individual resistive pulses from translocation of Fab fragments through a bilayer-coated nanopore containing 99.2 mol% POPC and 0.8 mol% Rh-PE in the bilayer coating (but no biotin-PE) and analysis of  $t_d$  and  $\Delta I$  of these resistive-pulses. **c**, Individual resistive pulses from translocation of Fab fragments through a bilayer-coated nanopore containing 0.15 mol% biotin-PE,  $\sim 99$  mol% POPC, and 0.8 mol% Rh-PE and analysis of  $t_d$  and  $\Delta I$  of these resistive-pulses. **d**, Individual resistive-pulses from translocation of Fab fragments through a nanopore coated with a bilayer of increased viscosity (containing 0.15 mol% biotin-PE, 49.5 mol% POPC, 49.5 mol% cholesterol, and 0.8 mol% Rh-PE) and analysis of  $t_d$  and  $\Delta I$  of these resistive-pulses. Distributions of  $t_d$ , except the incomplete distribution in **b**, were fit with equation (S10) as described in Supplementary Section S5.4 and S7.1. The experiments were performed with the nanopore shown in Supplementary Fig. S2c. The recording buffer contained 2.0 M KCl and 10 mM HEPES buffered at a pH of  $7.4 \pm 0.1$ . Currents were recorded at an applied potential difference of  $-0.1 \text{ V}$ .

lipid bilayer concentrated the proteins from solution onto the surface of the fluid bilayer *via* protein-ligand binding and that these surface bound proteins translocated through the pores at a higher frequency than proteins from the bulk electrolyte. Furthermore, it suggests that the resistive pulses we observed with bilayer-coated nanopores containing biotin-PE were mostly (> 90%) due to the movement of protein-biotin-PE complexes within the bilayer coating of the nanopore.

In the absence of biotin-PE in the bilayer coating, we expected the translocation of proteins through the pore to occur faster than in pores that were coated with a bilayer containing biotin-PE since in the latter case the viscosity of the bilayer can reduce the translocation speed of proteins bound to lipids. As a result, we expected to observe reduced values of  $t_d$  and attenuated values of  $\Delta I$  compared when biotin-PE was not used in the bilayer coating. Due to the non-Gaussian distributions of  $t_d$ , we compared the values of translocation times,  $t_d$ , that we observed most frequently in each distribution of  $t_d$  values (*i.e.* the most probable value). For instance, the translocation of anti-biotin mAb through a bilayer-coated pore without biotin-PE lipids was significantly faster ( $t_d \approx 22 \mu\text{s}$ ) than the translocation through the same pore with a bilayer coating that contained biotin-PE ( $t_d = 54 \pm 8 \mu\text{s}$ ) (Fig. S11). The translocation time of  $22 \mu\text{s}$  was below the lower limit of accurate quantification of  $t_d$ , and consequently, we obtained reduced values of  $\Delta I$  when the bilayer coating did not contain biotin-PE (Fig. S11c). Thus, we did not resolve a complete distribution of  $\Delta I$ , and we observed few values of  $\Delta I$  (<10%) larger than 500 pA (Fig. S11c).

We obtained similar results from analyzing resistive pulses due to the translocation of Fab fragments; the translocation of Fab fragments through a bilayer-coated pore without biotin-PE lipids was faster ( $t_d \approx 20 \mu\text{s}$ , Fig. S12b) than the translocation through the same pore with a

bilayer coating that contained biotin-PE ( $t_d = 78 \pm 5 \mu\text{s}$ , Fig. S12c). Again, we observed reduced values of  $\Delta I$  and an incomplete distribution of  $\Delta I$  (Fig. S12b) when the bilayer did not contain biotin-PE lipids. In contrast, when the bilayer coating contained biotin-PE, the increased translocation time of Fab through the nanopore resulted in a fully resolved distribution of  $\Delta I$  with an average value of  $254 \pm 39 \text{ pA}$  (Fig. S12c). Using equation (2) from the main text, we estimated a volume of  $172 \pm 31 \text{ nm}^3$  for the Fab fragments; the expected volume from literature is  $\sim 140 \text{ nm}^3$ <sup>20</sup>. Together, these results provide evidence that the local viscosity of the bilayer coating in combination with lipids presenting ligands provides an effective novel strategy for increasing the translocation time of specific proteins that are bound to lipid-anchored ligands.

To further increase the translocation time of Fab fragments, we generated a bilayer coated nanopore that contained biotin-PE and cholesterol. The presence of cholesterol in a lipid bilayer can increase its viscosity significantly<sup>13</sup>. We hypothesized that the translocation of Fab through this bilayer-coated nanopore would be slower than with a bilayer coating of purely POPC and biotin-PE. For these experiments, we formed the bilayer coating from liposomes prepared with 0.15 mol% biotin-PE, 0.8 mol% Rh-PE, 49.5 mol% POPC, and 49.5 mol% cholesterol. As expected, in the presence of anti-biotin Fab fragments, we observed translocation times ( $t_d = 175 \pm 4 \mu\text{s}$ , Fig. S12d) approximately twice as long as with bilayers that did not contain cholesterol ( $t_d = 78 \pm 5 \mu\text{s}$ , Fig. S12c). We obtained a value of  $\Delta I$  of  $275 \pm 29 \text{ pA}$ , which corresponds to a volume of  $178 \pm 19 \text{ nm}^3$  (Fig. S12d). Given that the reported volume of Fab fragments are  $\sim 140 \text{ nm}^3$ , these results suggest, once again, that a bilayer coating with increased viscosity made it possible to resolve translocation events of individual proteins completely in time and that this capability makes it possible to determine the volume of Fab fragments accurately.

*S5.4 Comparison of Diffusion Coefficients of Lipids and Diffusion Coefficients of Proteins in the Nanopore.*

We expected the diffusion coefficient of the lipids in the bilayer,  $D_L$ , and the diffusion coefficient of the proteins in the nanopore,  $D_P$ , to have similar values since diffusion coefficients of lipid-anchored proteins are determined by the diffusion coefficients of their lipid anchor in a lipid bilayer<sup>21-23</sup>. Table 2 in main text compares  $D_L$  to  $D_P$  using equation 3 from the main text to calculate  $D_P$  based on measured  $t_d$  values. For this comparison, we used the most probable value of  $t_d$  and the known charge of the protein to calculate the diffusion coefficient,  $D_P$ . Recent work by Talaga and Li enables an additional method for determination of  $D_P$  by fitting individual distributions of  $t_d$  values to a biased diffusion first passage time model developed by these authors<sup>24</sup>. Here, we compare diffusion coefficients obtained by these fits to the entire distribution of  $t_d$  values with diffusion coefficients of the lipids,  $D_L$ , determined by FRAP.

The model developed by Talaga and Li is shown in equation (S10); this function describes the distribution of values of  $t_d$  that result from the translocation of charged proteins through a nanopore in the presence of an electric field<sup>24</sup>:

$$P(t_d) = \frac{(vt_d + l_p) \times e^{-\frac{(l_p - vt_d)^2}{4Dt_d}}}{t_d \times \sqrt{4Dt_d} \pi} \tag{S10}$$

Here,  $v$  ( $\text{m} \times \text{s}^{-1}$ ) is the electrophoretic drift velocity and  $D$  ( $\text{m}^2 \times \text{s}^{-1}$ ) is the diffusion coefficient of the protein *within the nanopore*. Briefly, this equation assumes that a particle (or protein) moves in one dimension with an electrophoretic mobility  $u_e$  ( $\text{m}^2 \times \text{V}^{-1} \times \text{s}^{-1}$ ) and that its motion is driven by a linear electric field,  $\varepsilon$  ( $\text{V} \times \text{m}^{-1}$ ), which results in the electrophoretic drift velocity,  $v = \varepsilon \times u_e$ . It also assumes that the protein moves from a starting point (signified in time by the

beginning of the resistive pulse) to an infinite sink that is a distance  $l_p$  away (signified in time by the end of the resistive pulse). Further details on the derivation can be found in the article by Talaga and Li<sup>24-26</sup>.

Since the values of  $t_d$  result from the translocation of a protein, a best-fit analysis of the distribution of  $t_d$  values from protein translocation experiments with equation (S10) provides the diffusion coefficient of the proteins in the nanopore (i.e.  $D = D_p$ ). As shown in Table S2, the values of  $D_p$  were similar to values of  $D_L$  when the bilayer coating contained biotin-PE lipids and when the proteins were able to bind to the lipid-anchored biotin moiety. Typically we observed values of  $D_p$  that were within  $\pm 31\%$  of the value for  $D_L$ , with a maximum deviation of  $+117\%$ . When the bilayer coating did not contain biotin-PE or when the protein did not bind to the lipid-anchored biotin moiety (i.e. in the presence of excess biotin free in solution), this analysis determined values of  $D_p$  that were at least 3-fold greater than the value of  $D_L$ . Although these  $D_p$  values were only semi-quantitative due to the incomplete distribution of such short  $t_d$  values, they indicate that the diffusion coefficient of unbound proteins through the nanopore did not depend on the viscosity of the bilayer coating. Moreover, the agreement between  $D_p$  of proteins bound to a lipid-anchored ligand and  $D_L$  supports the hypothesis that the fluidity of the bilayer coating determined the translocation time of lipid-anchored proteins through the nanopores. These results provide further evidence for the formation of a fluid, bilayer coating within the nanopore.

**Table S2.** Comparison of diffusion coefficients of lipid-anchored proteins within the nanopore,  $D_p$ , determined by equation (S10) with diffusion coefficients of lipids in the bilayer coating,  $D_L$ .

Protein	Lipid Bilayer	$D_L^a$ ( $\text{nm}^2 \mu\text{s}^{-1}$ )	$D_p^b$ ( $\text{nm}^2 \mu\text{s}^{-1}$ )	$\Delta_D^c$ %
SA <sup>d</sup>	POPC + biotin-PE	1.13 ± 0.13	1.4 ± 0.1	+24
SA <sup>d</sup>	DΔPPC + biotin-PE	1.56 ± 0.16	1.7 ± 0.1	+9
mAb <sup>e</sup>	POPC + biotin-PE	1.29 ± 0.13	2.8 ± 0.2	+117
Fab <sup>e</sup>	POPC + biotin-PE	1.27 ± 0.13	1.7 ± 0.1	+31
Fab <sup>e</sup>	50 mol% POPC and 50 mol% cholesterol + biotin-PE	0.31 ± 0.03	0.6 ± 0.05	+100

<sup>a</sup>  $D_L$  was calculated based from the FRAP method as described in Supplementary Section S2.

<sup>b</sup> Diffusion coefficient of the protein,  $D_p$ , in the nanopore as obtained from the best-fit of the cumulative distributions of  $t_d$  values (see section S7.1) to equation (S13), which is the integrated form of equation (S10).

<sup>c</sup> Delta ( $\Delta_D$ ) was calculated by:  $100 \times (D_p - D_L) / D_L$

<sup>d</sup> Experiments were performed with the nanopore shown in Supplementary Figure S2b.

<sup>e</sup> Experiments were performed with the nanopore shown in Supplementary Figure S2c.

### Section S6. Translocations of Non-Spherical Proteins Generate Broad Distributions of $\Delta I$

Figure 4 in the main text shows that the distributions of  $\Delta I$  values for streptavidin and Fab fragments were significantly narrower than the distribution for the IgG antibodies. On first sight, the two maxima in Fig. 4c might be attributed to a contamination by other proteins in the solution of anti-biotin IgG antibodies. Closer inspection of the data reveals, however, that these contaminants would have to bind specifically to biotin, since neither of the two peaks in Fig. 4c were present in control experiments with pores that were coated with the same bilayer but without biotinylated lipids (Supplementary Fig. S11). The broad distribution in Fig. 4c was, however, not caused by a contamination of anti-biotin Fab fragments in the solution of anti-biotin IgG antibodies because Fab fragments would result in a narrow peak in the distribution with a most frequently observed  $\Delta I$  value  $\sim 0.25$  nA (Fig. 4b), while the two maxima in Fig. 4c were located at  $\Delta I$  values of  $\sim 0.4$  nA and  $\sim 1.0$  nA. Therefore, we attribute the broad distribution



of  $\Delta I$  values in Fig. 4b primarily to the complex molecular shape of IgG antibodies ( $\gamma \neq 1.5$ ) compared to the approximately spherical shape ( $\gamma \approx 1.5$ ) of streptavidin and Fab fragments. In order to provide an estimate for the shape factor of IgG antibodies, we considered their thickness of 2.4 nm and volume of  $347 \text{ nm}^3$ <sup>27</sup> and approximated their shape by an oblate spheroid (*i.e.*, by a lentil-shaped particle) with a volume equal to IgG antibodies and a pole-to-pole diameter,  $A$ , equal to the thickness of IgG antibodies ( $A = 2.4 \text{ nm}$ ). This approximation yields an oblate spheroid with an equatorial diameter,  $B$ , of 16.6 nm. The shape factor,  $\gamma$ , of an oblate spheroid with diameters  $A$  and  $B$  depends on the orientation in which it translocates through the pore<sup>2</sup>. Figure S13 illustrates this orientation dependence of  $\gamma$  graphically. For the two extremes of translocation with the pole-to-pole axis of the spheroid oriented perpendicular to the length axis of the pore, Grover *et al* predicted  $\gamma = 1.1$  and for translocation with the equatorial axis oriented perpendicular to the length axis of the pore, they predicted  $\gamma \approx 5.0$ <sup>2</sup>. The two dashed red lines in Fig. 4c in the main text indicate  $\Delta I$  values for these two values of  $\gamma$  as predicted theoretically by equation (2) in the main text for oblate spheroids with diameters  $A$  and  $B$  and a volume of  $347 \text{ nm}^3$ . Since these two values of  $\Delta I$  represent the extremes with regard to the orientation during translocation, the majority of the experimentally observed values of  $\Delta I$  would be expected to lie between these extremes. Fig. 4c confirms this expectation and provides the first experimental support that resistive pulse analysis may yield information about the shape (based on the distribution of  $\Delta I$  values) and orientation (based on the individual  $\Delta I$  value) of proteins with known volumes during their translocation, as predicted theoretically by Grover *et al* in 1969<sup>2</sup>. Previously, Mathe *et al.* observed orientation dependent translocation in nanopore-based DNA experiments through  $\alpha$ -hemolysin pores<sup>28</sup> and Akeson *et al.* observed large variations in  $\Delta I$  for the same population of nucleic acids due to various physical processes<sup>29</sup>.

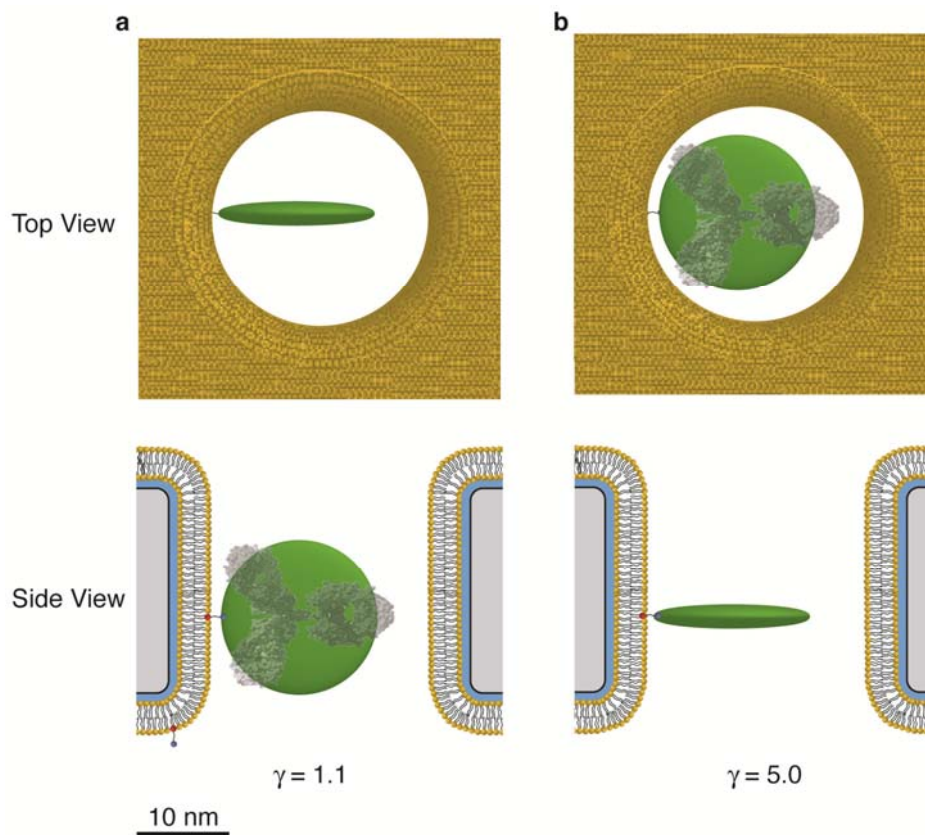


**Figure S13 | Two extremes of possible orientations of an IgG antibody, approximated by an oblate spheroid, during its translocation through a nanopore.** **a**, Cartoon illustrating the translocation of an oblate spheroid with its pole-to-pole axis oriented perpendicular to the length axis of the pore; this orientation would result in a shape factor,  $\gamma$ , of 1.1. **b**, Illustration of the same oblate spheroid as in **a** but translocating through the pore with its equatorial axis oriented perpendicular to the length axis of the pore; this orientation would result in a shape factor,  $\gamma$ , of 5.0. Note that the illustration is drawn to scale and that the nanopore was drawn to match the dimensions of the pore used for the experiments in Fig. 4c of the main text. A scaled space-filling model of an IgG antibody<sup>30</sup> with a volume of 347 nm<sup>3</sup> overlays the oblate spheroid with the same volume.

As mentioned before, the two orientations in Fig. S13 represent the two extremes, realistically a lipid-anchored protein will probably not move through the pore in only one orientation but in many orientations as it rotates around its lipid anchor. To examine the

possibility of rotation, we estimated the time it would take an antibody to rotate  $2\pi$  radians ( $360^\circ$ ) around one axis based on equations (S11) and (S12)<sup>31</sup>:

$$\langle \theta^2 \rangle = 2 D_r t, \quad (11)$$

where  $\theta$  (rad) is the degrees of rotation,  $D_r$  ( $\text{rad}^2 \text{s}^{-1}$ ) is the rotational diffusion coefficient and,  $t$  is (s) the time. Using the effective radius of an IgG antibody determined from diffusion coefficient measurements<sup>32</sup> ( $R_{\text{eff}} = 5.5 \text{ nm}$ ), we estimated  $D_r$  for an IgG antibody from equation S12<sup>31</sup>:

$$D_r = \frac{k_B T}{f_r} = \frac{k_B T}{8\pi\eta R^3}, \quad (12)$$

where  $k_B$  ( $\text{J K}^{-1}$ ) is the Boltzmann constant,  $T$  (K) is the temperature, and  $f_r$  is the rotational friction coefficient. Based on these calculations, which were derived for spherical particles, we estimated that the average time for an antibody to complete one rotation would be  $\sim 18 \mu\text{s}$ . We also calculated the time for one rotation of a disk with a similar size to an IgG antibody and obtained a value of  $\sim 26 \mu\text{s}$ <sup>31</sup>. These times are approximately one third of the translocation time of the antibody through the nanopore (Fig. 3c in the main text). Consequently, the rotation of the antibody while inside the nanopore may result in a value of  $\gamma$  that is the average of the two extreme values, which would yield  $\langle \gamma \rangle = 3.1$ . This hypothesis is consistent with the peak at  $\Delta I \sim 1.0 \text{ nA}$  in the distribution of  $\Delta I$  values for the mAb as indicated by the red dashed line in Fig. 4c of the main text. The additional peak in Fig. 4c at  $\Delta I \sim 0.4 \text{ nA}$  might be due to factors that are not considered in equations (S11) and (S12). For instance, the rotational diffusion coefficient predicted by equation (S12) assumes a spherical protein that is free in solution. Here, the protein was not spherical and attached to a surface inside the confined volume of a nanopore. All three effects likely increase the average time it takes for the antibody to complete a full rotation. This increased time in combination with steric effects inside the confined volume of the nanopore

may result in a preferred orientation of the antibody in the nanopore (i.e. Fig. S13a) that is maintained throughout most of the translocation time. Another possibility is the alignment of the antibody within the electric field due to a dipole moment within the molecule. Due to the shape of the IgG antibody, such an alignment would be most likely along its length axis and result in the orientation of the mAb shown in Fig. S13a and a peak in the  $\Delta I$  distributions at a value of  $\gamma$  of approximately 1.1. In addition, hydrodynamic effects as a result of rotation may drive antibodies towards the wall of the pore, which would also favor the orientation shown in Fig. S13a.

To provide a second example of a broad distribution of  $\Delta I$  obtained with a non-spherical protein, we employed a bilayer coated nanopore containing biotin-PE lipids in the bilayer coating, streptavidin, and a biotinylated IgG antibody (anti-catalase antibody, AbCam<sup>®</sup>). In this experiment, streptavidin bound to the biotin-PE lipids and translocated through the pore resulting in resistive pulses with small values of  $\Delta I$  (Fig. S14a). Subsequent addition of the biotinylated-IgG antibody and the translocation of the lipid-anchored, streptavidin-IgG complex returned large values of  $\Delta I$  and an even broader distribution of values for  $\Delta I$  (Fig. S14b) than those from the translocation of the anti-biotin mAb (Fig. S11a and Fig. 4c from the main text). We expected this result since the shape of the streptavidin-IgG complex deviates even further from a spherical shape than an IgG antibody. We approximated the streptavidin-IgG complex as an oblate spheroid with a pole-to-pole diameter of 2.4 nm and an equatorial diameter of 18.8 nm; the shape factor of such an oblate spheroid would be  $\gamma = 1.1$  when the pole-to-pole axis is oriented perpendicular to the length axis of the pore and  $\gamma = 5.5$  when the equatorial axis is oriented perpendicular to the length axis of the pore. Figure S14b shows that approximately 95% of the

values for  $\Delta I$  were between the expected  $\Delta I$  for the protein complex given the molecular volume of the complex and these values for  $\gamma$ .

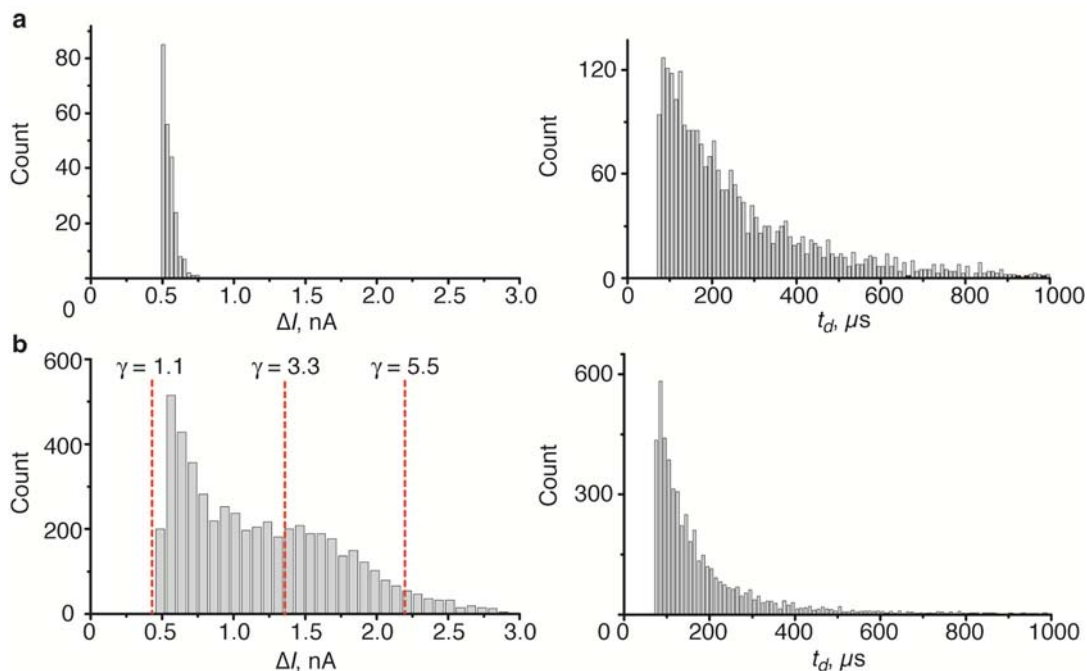


**Figure S14 | Translocation of non-spherical lipid-anchored streptavidin-IgG complexes resulted in broad distributions of  $\Delta I$  due to the various orientations the complex could assume inside the nanopore.** **a**, Distributions of  $\Delta I$  and  $t_d$  resulting from the translocation of streptavidin while bound to biotin-PE lipids in the bilayer coating of a nanopore. **b**, Distributions of  $\Delta I$  and  $t_d$  after the addition of a biotinylated polyclonal, IgG antibody against catalase. Note that before recording resistive pulses, the electrolyte solutions were thoroughly rinsed to remove unbound proteins from the solution. The bilayer coating in this experiment contained 0.15 % biotin-PE, 0.8% Rh-PE, and ~99% POPC. The nanopore had a diameter of 36 nm and a length of 26 nm with the bilayer coating.

## Section S7. Determining the Most Probable Value of $t_d$ and its Error

### *S7.1 Determining the Most Probable $t_d$ Value and its Error by Fitting Cumulative Distributions of $t_d$ Values*

In the main text, we report the most frequently observed value of  $t_d$ , located at the absolute maximum of each distribution of measured  $t_d$  values. We quantified these most probable values of  $t_d$  by generating cumulative distributions of measured  $t_d$  values. To generate cumulative distributions we summed the relative number of observations that occurred at or below a specified  $t_d$  value (x-axis), thereby effectively integrating the data<sup>33</sup>. Cumulative distributions are advantageous compared to the histograms shown in Fig. 3 in the main text because they are generated from all  $t_d$  values without binning the data<sup>33</sup>. To fit these cumulative distributions we integrated equation (S10) to obtain equation (S13) and fit the cumulative  $t_d$  data to this equation:

$$A(t_d) = \frac{1}{2} \operatorname{erfc} \left[ \frac{(l_p - vt_d)}{2\sqrt{Dt_d}} \right]. \quad (\text{S13})$$

Figure S15 shows several cumulative distributions of  $t_d$  values that we obtained from translocation events of mAb through the pore while we applied different voltages across the pore. Figure S15 also shows the corresponding best fits of equation (S13) to the data in these distributions.

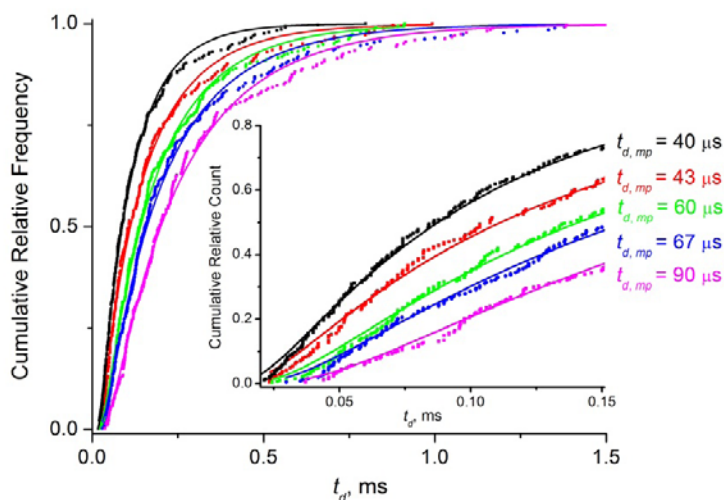


**Figure S15 | Cumulative distributions of  $t_d$  obtained from translocation events of mAb at different applied voltages.** Distributions of  $t_d$  values were determined from recording translocation events of mAb while applying potential differences of 120 mV (—), 100 mV (—), 80 mV (—), 70 mV (—), and 60 mV (—) across the chip. The inset shows the distributions over the range of  $t_d$  values of 20  $\mu$ s to 150  $\mu$ s. Best curve fits of this data to equation (S13) determined the most probable values of  $t_d$  ( $t_{d, mp}$ ) in order of decreasing applied potential difference: 40  $\mu$ s, 43  $\mu$ s, 60  $\mu$ s, 67  $\mu$ s, and 90  $\mu$ s.

To determine the most probable  $t_d$  value for a given distribution, we set the second derivative of the fitted equation (S13) equal to 0 and solved for  $t_d$ . The most probable  $t_d$  values determined from the cumulative distributions shown in Figure S15 are plotted in Figure S16 in Section S8.1. To report an error for each most probable  $t_d$  value, we varied the fitting parameters, including the length of the nanopore ( $l_p$ ) and the diffusion coefficient ( $D_L$ ), by their measured error and reported the maximum deviation in  $t_d$ . The maximum error in  $l_p$ , as estimated from the data in Fig. 1C in main text, was  $\pm 1$  nm while the maximum error of diffusion coefficients of lipids in supported lipid bilayers as determined by FRAP was  $\pm 10\%$ <sup>13</sup>.

This method resulted in most probable  $t_d$  values with errors that ranged from  $\pm 2\%$  to  $\pm 23\%$  of the most probable value of  $t_d$ .

Figure S15 shows that cumulative distributions whose most probable  $t_d$  values differed by only  $3\ \mu\text{s}$  could be resolved (see the black and red data) if the experiment was performed on *the same chip*, with the same bilayer, and under the same experimental conditions. This high resolution is likely to result from errors in  $l_p$  that are expected to have nearly the same systematic error for all recordings and would therefore be expected to be significantly smaller than  $\pm 1\ \text{nm}$ . The errors of up to  $\pm 23\%$  of the most probable  $t_d$  values reported above refer to separate experiments, possibly with different chips, when the chips were cleaned and fresh bilayers were formed between each experiment.

### S7.2 Determining the Most Probable $t_d$ Value by Fitting Histograms of $t_d$ Values

In the experiments for determining the most probable values of  $t_d$  for the translocation of streptavidin at different pH values of the electrolyte (Fig. 5 in the main text), we found that a few of the cumulative  $t_d$  distributions could not be fit very well with equation (S13). Therefore we determined the most probable value of  $t_d$  from these distributions with fits of equation (S14) to  $t_d$  histograms, which returned the location of the maximum in the histograms:

$$y = y_o + A e^{\left( -e^{\frac{(x-x_c)}{w}} - \frac{(x-x_c)}{w} + 1 \right)} \quad (\text{S14})$$

In this equation  $y_o$  is the baseline,  $A$  is the amplitude of the peak,  $x_c$  is the  $x$ -value at the center of the peak (i.e. the most probable value of  $t_d$ ), and  $w$  is the width of the distributions. Based on the results of this fit to the distributions of  $t_d$ , we reported the value of  $x_c$  and its error from the fit as the most probable  $t_d$  value with its associated error. To determine if the value of  $x_c$  was sensitive



to the size of the bins in the  $t_d$  histograms, we generated histograms with different bin-widths from  $t_d$  values obtained [streptavidin](#). In all cases the first bin began at 25  $\mu\text{s}$  since this value represents the lower limit for accurate detection and quantification of  $t_d$  (See Supplementary Section S9). Figure [S16](#) shows the resulting histograms from bin widths of 15  $\mu\text{s}$ , 30  $\mu\text{s}$ , and 50  $\mu\text{s}$ . In all three cases, the most probable  $t_d$  values (i.e. the value of  $x_c$ ) determined by the best curve fits of equation (S14) to  $t_d$  histograms were within error of each other (with maximum deviations of 6  $\mu\text{s}$ ), demonstrating that this method of fitting distributions of  $t_d$  values for determining the most probable  $t_d$  value was not sensitive to the binning method in a range of bin widths from 15 to 50  $\mu\text{s}$ .

One of the advantages of using the most probable value of  $t_d$  for quantitative analysis compared to using, for instance, the average value of  $t_d$ , is that the absolute maximum in each distribution can be determined with high accuracy and small errors ([smaller than 23% of the most probable value of  \$t\_d\$](#) ) from fits to histograms of  $t_d$ . This approach of determining the location of the absolute maximum is not sensitive to the possible presence of small sub-peaks in  $t_d$  histograms such as those present in some  $t_d$  distributions in Fig. 3 in the main text.

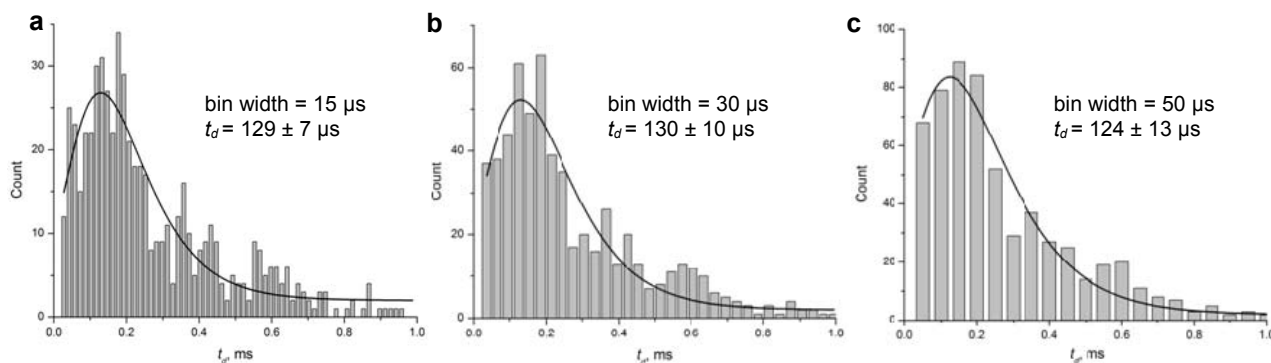


**Figure S16 | Effect of different bin-widths for determining the most frequently observed value of  $t_d$  based on best curve fits of  $t_d$  data in histograms to equation (S14).** Different bin-widths of a) 15  $\mu$ s, b) 30  $\mu$ s, and c) 50  $\mu$ s were used to produce these histograms from  $t_d$  values that were measured from translocation events of streptavidin in an electrolyte with pH = 6.6. These  $t_d$  histograms were fit with equation (S14) using the non-linear curve fitting function of the software OriginPro 8 with its so called “Extreme Function”.

## Section S8. Calculating the Charge of Proteins from the Translocation Time of Lipid-Anchored Proteins

### S8.1 Derivation of equation (3) in the main text

Based on recent work by Sexton *et al*, we developed the simplest possible model that yields a relationship between  $t_d$ , the lateral diffusion coefficient of the lipids in the bilayer coating,  $D_L$ , and the net charge of a protein,  $|z| \times e$ , where  $z$  (unitless) is the net valency of the charge on the protein and  $e$  (C) is the elementary charge of an electron<sup>34</sup>. This model assumed that the only driving force,  $f$  (N), acting on a charged, translocating protein is exerted by the electric field that drops inside the pore; it also assumed that inside of cylindrical nanopores the voltage  $V_p$  (V) drops linearly along the length of the pore,  $l_p$  (m):

$$f = |z|e \frac{V_p}{l_p}. \tag{S15}$$

Note that  $V_p$  refers only to the part of the total applied voltage,  $V_a$ , that drops inside the pore, and it can be calculated by  $V_p = V_a \times R_p / R_{total}$  (see Supplementary Equations (S3) and (S6)). Based on these assumptions, the charged protein experiences a constant force opposed by a viscous drag inside the pore, leading to a constant net electrophoretic drift velocity,  $v$  ( $\text{m s}^{-1}$ ):

$$v = \frac{l_p}{t_d} = \frac{f}{\zeta}, \quad (\text{S16})$$

where  $\zeta$  ( $\text{kg s}^{-1}$ ) represents the viscous friction coefficient. Assuming that, for lipid-anchored proteins,  $\zeta$  is dominated by the lipid anchor in the bilayer<sup>21-23</sup>, it can be expressed by the Stokes-Einstein relationship:

$$\zeta = \frac{k_B T}{D_L}, \quad (\text{S17})$$

where  $k_B$  ( $\text{J K}^{-1}$ ) is the Boltzmann constant,  $T$  (K) is temperature, and  $D_L$  ( $\text{m}^2 \text{s}^{-1}$ ) represents the lateral diffusion coefficient of lipids in the bilayer. Combining equations (S15)-(S17) yields the desired functional relationship between  $t_d$ , the diffusion coefficients of the lipids in the bilayer coating, and the net charge of a translocating protein:

$$t_d = \frac{l_p^2 k_B T}{|z| e V_p D_L}. \quad (\text{S18})$$

This equation is the same as equation (3) in the main text.

In order to validate this model and the resulting equation (S18), we analyzed translocation events of streptavidin molecules through bilayer-coated pores with biotin-PE lipids while employing electrolyte solutions of various pH to vary the value of  $|z|$  according to Sivasankar et al<sup>35</sup>. Figure 5 of the main text shows that equation (S18) accurately predicted  $t_d$  as a function of  $|z|$  and could be used to determine parameters such as  $D_L$ ,  $l_p$ , or  $|z|$ .

We further validated equation (S18), which is equation (3) in the main text, by determining the most probable  $t_d$  values from translocation events of the IgG antibody as a function of the voltage drop inside the nanopore,  $V_p$ . Fig. S17 illustrates that  $t_d$  was indeed inversely proportional to  $V_p$  as predicted by equation (S18). Moreover, fitting equation (S18) to the data in Fig. S17 revealed a net charge of the antibody of  $z = -4.2 \pm 0.5$  with  $z$  as the only fitting parameter. This value compares well to the value of  $z = -3.6 \pm 2.3$  determined by capillary electrophoresis (Section S8.2). We also used equation S18 to calculate a net average charge for the Fab fragment of  $-5.4 \pm 0.6$  based on the most frequently observed  $t_d$  value in Fig. 3b of the main text. This value is comparable to the charge that we determined by capillary electrophoresis ( $z = -4.3 \pm 0.4$ ) or by fits to the distributions of  $t_d$  ( $z = -2.9 \pm 0.6$ ) (see Sections S8.2 and 8.3). As a result, we reported a range for the values of  $z$  in the main text.

Note that in all experiments, we assumed that the pH value inside the nanopore was the same as the pH value in the bulk electrolyte solution. Since we carried out all protein translocation experiments in nanopores that were coated with electrically neutral phosphatidylcholine bilayers and since the KCl concentration of the electrolyte in these experiments was 2.0 M, we did not expect significant differences between the pH value inside the pore and the value in the bulk solution.

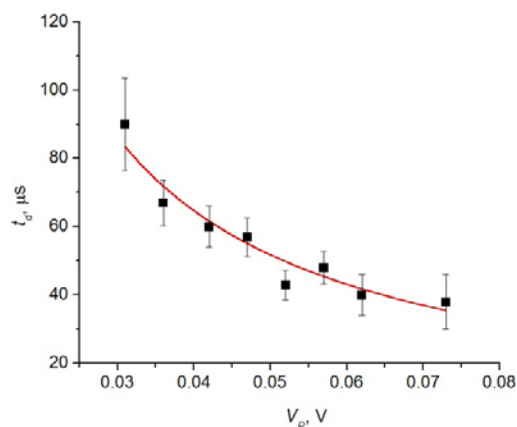


**Figure S17 | Most probable  $t_d$  values for the monoclonal anti-biotin IgG<sub>1</sub> antibody (mAb) as a function of the voltage drop,  $V_p$ , across a bilayer-coated nanopore containing biotin-PE.** The red curve was obtained by a best fit of equation (S18) to the data with  $z$  as the only fitting parameter. The fit returned a value for  $z$  of  $-4.2 \pm 0.5$  with  $R^2 = 0.94$  ( $N = 8$ ). The error bars of the most probable  $t_d$  values in this plot are likely overestimates that are based on an  $l_p$  of  $\pm 1$  nm since all of these recordings were performed on the same chip with the same bilayer and the variations in  $l_p$  between current recordings are more likely to be  $\pm 0.2$  nm due to fluctuations in the thickness of the water layer and lipid bilayer. The bilayer coating in this experiment contained 0.15% biotin-PE, 0.8% Rh-PE, and ~99% POPC. After the bilayer coating, the nanopore had a diameter of 36 nm and a length of 24 nm.

### S8.2 Capillary Electrophoresis for Determining the Net Charge of Proteins

To provide independent evidence that values of  $t_d$  can be used to calculate the net charge of proteins used in this work, we determined the net charge of streptavidin (SA), anti-biotin antibody Fab fragments, and monoclonal anti-biotin IgG antibodies (mAb) from capillary electrophoresis (CE) experiments. Figure S18a, b shows electropherograms for SA and Fab that we obtained using a CE instrument from Hewlett-Packard equipped with a UV absorbance detector. In each electropherogram, two peaks were present due to a transient increase in the absorbance within the light-path of the detector near the end of the capillary. The first peak was

due to the so-called neutral marker (a small molecule with a net charge of zero), 4-methoxybenzyl alcohol, and the second peak was attributed to the protein. The difference between the elution time for the neutral marker,  $t_{NM}$  (s), and the elution time,  $t_A$  (s), for a spherical protein is given by equation (S19)<sup>36</sup>:

$$z = \frac{L_T L_D 6 \pi \eta R \left( \frac{1}{t_A} - \frac{1}{t_{NM}} \right)}{V_A e}, \quad (19)$$

where  $L_T$  (m) is the total length of the capillary,  $L_D$  (m) is the length of the capillary to the detector,  $\eta$  (Pa  $\times$  s) is the viscosity of the electrolyte (calculated in this work from equation (S8)),  $R$  (m) is the effective radius of the protein,  $V_A$  (V) is the applied potential difference across the capillary, and  $e$  (C) is the elementary charge of an electron. Based on the volume of the proteins, we estimated an effective radius for SA of 2.9 nm (corresponding to 105 nm<sup>3</sup>) and for Fab of 3.2 nm (corresponding to 140 nm<sup>3</sup>). For the mAb, we used an effective radius of 5.5 nm that Jossang *et al.* determined from the diffusion coefficient of IgG antibodies<sup>32</sup>. Table S3 lists the calculated charge of SA and Fab that we determined from these CE experiments and compares these values to the ones determined from fits to the distributions of  $t_d$  values obtained during the nanopore translocation experiments.

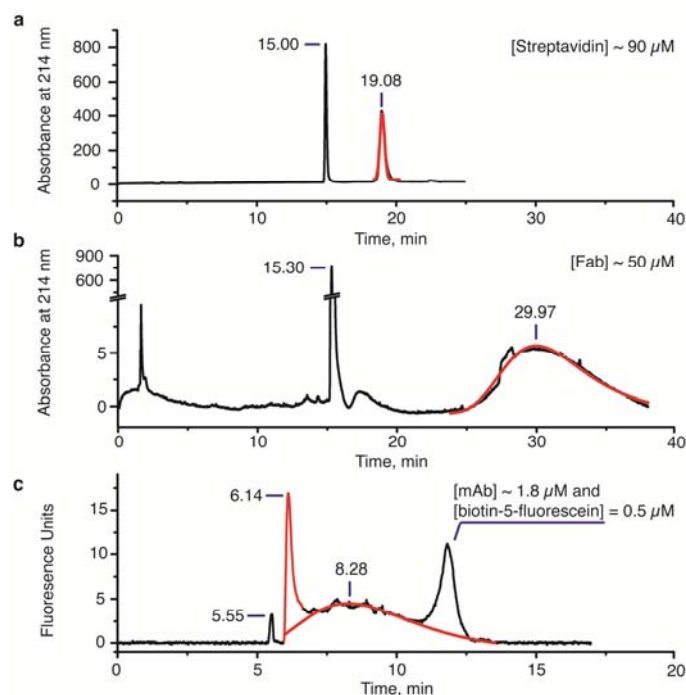


**Figure S18 | Capillary electropherograms for determining the charge of the proteins used in this**

**work.** **a, b,** Electropherograms obtained with a CE instrument equipped with UV detection. Protein samples were prepared in PBS at pH 7.4 and included the neutral marker, 4-methoxybenzyl alcohol. The neutral marker appeared at 15–15.5 min and is labeled in the figure. Peaks due to the protein are shown in red and the time of each peak's maxima is indicated in the figure. The capillary was a fused silica capillary with a total length of 64.5 cm and an internal diameter of 50 μm. The length of the capillary to the detector was 56 cm and the total applied voltage was 15 kV. The temperature of the capillary was maintained at 25 °C **c.** Electropherogram obtained with a CE instrument equipped with fluorescence excitation at 490 nm and detection at 540 nm. The protein sample was prepared in PBS at pH 7.4 and included the zwitterionic fluorophore, rhodamine B, which served as the neutral fluorescent marker. The sample contained 1.8 μM of the anti-biotin IgG mAb and 0.5 μM of biotin-5-fluorescein, with a net charge of  $z = -1$ . The capillary was a fused silica capillary with a total length of 30 cm and an internal diameter of 50 μm. The length of the capillary to the detector was 20 cm and the total applied voltage was 7.0 kV. The temperature of the capillary in **c** was maintained at 28 °C Note that in all cases, the baseline of the electropherograms were adjusted.

Based on CE experiments, we measured slightly different values for the charge of SA than those reported by Sivasankar *et al*; these deviations increased as the pH decreased. These discrepancies are likely due to the difference in the charge of SA in solution compared the charge of SA bound to a surface by a biotin anchor. The reported pI of SA in solution is 6.3<sup>35</sup> while Sivasankar *et al*. reported a pI of SA bound to biotinylated lipids of 5-5.5 and Vlassioux *et al*. reported a pI of SA bound to immobilized biotin on a surface of ~5.5<sup>35,37</sup>. Since, the experimental conditions used by Sivasankar *et al*. were very similar to those used here (i.e. SA bound to biotinylated lipids in a lipid bilayer composed of lipids with a head group of phosphatidylcholine), we plotted  $t_d$  values in Fig. 5 of the main text *versus* the values reported by Sivasankar *et al*.

**Table S3.** Net valence,  $|z|$ , of the charge of proteins, diffusion coefficients of proteins within the nanopore,  $D_P$ , and diffusion coefficients of lipids in the bilayer coating,  $D_L$ .

Protein	Lipid Bilayer <sup>a</sup>	pH of electrolyte	$Z_{LITERATURE}$ <sup>35</sup>	$Z_{CE}$ <sup>b</sup>	$Z_{Td}$ <sup>c</sup>	$D_L$ <sup>d</sup> ( $\text{nm}^2 \mu\text{s}^{-1}$ )	$D_P$ <sup>c</sup> ( $\text{nm}^2 \mu\text{s}^{-1}$ )	$\Delta_D$ %
SA	POPC	7.4	$-1.9 \pm 0.4$	$-1.8 \pm 0.1$	$-0.8 \pm 0.2$	$1.13 \pm 0.13$	$1.4 \pm 0.1$	+24
SA	$\Delta$ PPC	7.4	$-1.9 \pm 0.4$	$-1.8 \pm 0.1$	$-1.1 \pm 0.2$	$1.56 \pm 0.16$	$1.7 \pm 0.1$	+9
SA	POPC	8.0	$-2.4 \pm 0.4$	$-2.8 \pm 0.3$	$-2.3 \pm 0.2$ <sup>f</sup>	$1.65 \pm 0.17$	$1.8 \pm 0.1$ <sup>f</sup>	+6
SA	POPC	7.1	$-1.7 \pm 0.4$	$-0.9 \pm 0.2$	$-1.6 \pm 0.1$ <sup>f</sup>	$1.65 \pm 0.17$	$1.7 \pm 0.1$ <sup>f</sup>	+6
SA	POPC	6.6	$-1.2 \pm 0.4$	$-0.7 \pm 0.2$	$-1.0 \pm 0.1$ <sup>f</sup>	$1.65 \pm 0.17$	$1.4 \pm 0.1$ <sup>f</sup>	-15
SA	POPC	6.1	$-0.8 \pm 0.4$	$-0.3 \pm 0.1$	$-0.9 \pm 0.1$ <sup>f</sup>	$1.65 \pm 0.17$	$1.0 \pm 0.1$ <sup>f</sup>	-39
SA	POPC	5.7	$-0.5 \pm 0.4$	—	$-0.9 \pm 0.1$ <sup>f</sup>	$1.65 \pm 0.17$	$1.2 \pm 0.1$ <sup>f</sup>	-21
Fab	POPC	7.4	—	$-4.3 \pm 0.4$	$-2.9 \pm 0.6$	$1.27 \pm 0.13$	$1.7 \pm 0.1$	+31
mAb	POPC	7.4	—	Peak 1: $-0.3 \pm 0.3$ Peak 2: $-3.6 \pm 2.3$	$-4.2 \pm 0.5$ <sup>e</sup>	$1.29 \pm 0.13$	$1.8 \pm 0.5$	+38

<sup>a</sup> All lipid bilayers also contained 0.15 – 0.4 mol% of Biotin-PE.

<sup>b</sup> Value of  $Z_{CE}$  determined by capillary electrophoresis from equation (S19).

<sup>c</sup> Value of  $Z_{Td}$  and  $D_P$  determined by fitting the cumulative distributions of  $t_d$  with equation (S13), in which  $v$  was described by equation (S20), with both  $Z_{Td}$  and  $D_P$  as fitting parameters.

<sup>d</sup> Values for  $D_L$  determined by FRAP as described in Supplementary Section S2.

<sup>e</sup> Value of  $z$  determined from the fit in Fig. S17.

<sup>f</sup> Values were determined by fitting equation S21 to histograms.



We performed a second set of CE experiments with a CE instrument from Beckman equipped with fluorescence detection. To detect proteins with this instrument, we incubated the anti-biotin IgG antibody with biotin-5-fluorescein prior to performing the CE experiment. Figure S18c shows the resulting electropherogram, which we used to calculate the net charge of the mAb. Since biotin-5-fluorescein presumably has a net charge of approximately -1 at pH 7.4, we subtracted 1 charge from the value of  $z$  determined with equation (S19) to calculate a net charge of the mAb. We observed two peaks in the presence of mAb, both of which grew in size with increasing concentrations of biotin-5-fluorescein. These two peaks did not overlap with the peak of unbound biotin-5-fluorescein and could therefore both represent the antibody-ligand complex. These two peaks after the neutral marker in Fig. S18c correspond to  $z$  values of  $-0.3 \pm 0.3$  and  $-3.6 \pm 2.3$  (Table S3).

### S8.3 Fitting Individual Distributions of $t_d$ with both $z$ and $D$ as Fitting Parameters

To determine if parameters such as  $|z|$  and  $D_L$  could be extracted from distributions of  $t_d$  such as those shown in Fig. 3 in the main text, we incorporated the net valence of the charge,  $|z|$ , of a protein into equation (S10) by combining it with equation (S20), which describes the electrophoretic drift velocity,  $v$ , based on equations (S15)-(S17):

$$v = \frac{|z|eV_p D}{l_p k_B T}. \quad (\text{S20})$$

Substituting equation (S20) into equation (S10) resulted in equation (S21), which permitted the determination of the diffusion coefficient of lipid anchored proteins,  $D_p$ , and the net valence of the charge of the proteins,  $|z|$ , in the nanopore based on best curve fits to individual distributions of  $t_d$ .

$$P(t_d) = \frac{\left[ \left( \frac{|z|eV_p D}{l_p k_B T} \right) t_d + l_p \right] \times e^{-\left[ l_p - \left( \frac{|z|eV_p D}{l_p k_B T} \right) t_d \right]^2 / 4Dt_d}}{t_d \times \sqrt{4Dt_d} \pi} \quad (\text{S21})$$

Table S3 compares the values of  $|z|$  obtained with this method to the literature values of  $|z|$  for SA, the values of  $|z|$  obtained with CE, the values of  $D_P$ , and the values of  $D_L$  for SA, mAb, and Fab. For Fab, values of  $|z|$  and  $D_P$  determined with equation (S21) from nanopore-based  $t_d$  distributions were in good agreement ( $\pm 39\%$ ) with the expected values as obtained from CE and from FRAP experiments.

For streptavidin, values of  $|z|$  determined by Sivasankar *et al.* agreed well with the values determined by fitting  $t_d$  distributions from translocation experiments with SA with equation (S21). The only exception was the experiment with streptavidin in an electrolyte with a pH of 5.7. The difference in the value of  $|z|$  of  $\Delta z = 0.4$  in the electrolyte with a pH of 5.7, is likely due to the reduced charge of SA at this pH ( $|z| = 0.5 \pm 0.2$ )<sup>35</sup>. This charge, which is close to neutral, presumably led to a shift from an electrophoretically dominated movement through the nanopore to a diffusion-dominated movement of SA. Consequently, a fraction of the recorded resistive pulses may have been due to partial translocation events (i.e. diffusion of SA into and out of the same side of the nanopore). Such events could be associated with shorter than expected values for  $t_d$ .

For the mAb, we observed two peaks in the CE data which corresponded to two different charges for the mAb. One of the peaks corresponds to a  $z = -3.6 \pm 2.3$ , which agrees well with the value of  $z = -4.2 \pm 0.5$  determined from the fit in Fig. S17. The second peak in the CE data corresponds to a  $z = -0.3 \pm 0.3$ . If the charge of the mAb would indeed be  $-0.3 \pm 0.3$ , then some proteins may only partially move through the nanopore (as discussed for SA at pH 5.7), which

may result in shorter than expected values for  $t_d$ . Consequently, the predictions of the charge of the mAb based on  $t_d$  values would calculate values for  $z$  that are larger than the true value. However, based on the results in Fig. S17, the charge of the mAb is likely to be  $z = -3.6$  rather than  $-0.3$ .

### Section S9. Data Acquisition and Analysis of Resistive Pulses for Protein Detection

We used Ag/AgCl pellet electrodes (Warner Instruments) to monitor ionic currents through electrolyte-filled nanopores with a patch-clamp amplifier (Axopatch 200B, Molecular Devices Inc.) in voltage clamp mode (i.e., at constant applied voltage). We set the analog low-pass filter of the amplifier to a cutoff frequency of 100 kHz. We used a digitizer (Digidata 1322) with a sampling frequency of 500 kHz in combination with a program written in LabView to acquire and store data.

To detect resistive pulses caused by the translocation of proteins through the nanopore, we applied a potential difference of  $\pm 0.1$  V across the nanopore. The polarity refers to the top fluid compartment that contained the protein while the other fluid compartment was always connected to ground. We recorded the resulting current with the maximum bandwidth of the recording setup (cut-off frequency,  $f_c \sim 50$  kHz)<sup>38</sup> and with a sampling frequency of 500 kHz using a custom program written in LabVIEW. To distinguish resistive pulses reliably from the electrical noise, we used the software PClamp (Molecular Devices Inc.) to determine the baseline of the current and to filter current recordings with a digital, Gaussian low-pass filter ( $f_c = 15$  kHz).

Using PClamp software, we performed a threshold-search for resistive pulses within the current recordings. We defined the start of a resistive pulse by a resistive decrease in the magnitude of the current past a threshold value that we set to  $5\times$  the standard deviation of the

noise of the baseline current. Based on this definition, typical threshold values ranged from 150 to 250 pA depending on the nanopore dimensions and the bilayer coating. The subsequent return of the current past a second threshold, which we set to one standard deviation of the noise in the baseline current, and toward the baseline value, marked the end of the resistive pulse. We confirmed that for the analysis of translocation events from streptavidin and Fab, this procedure returned the same  $t_d$  values as a method based on half-widths of resistive pulse recently reported by Talaga and Li<sup>24</sup>. Due to the large magnitude and magnitude variability of resistive pulses in the antibody experiments, we determined  $t_d$  values based on the half-width of resistive pulses from antibodies in a method similar to the approach described by Talaga and Li<sup>24</sup>. We defined  $\Delta I$  as the maximum deviation from the baseline current within the time,  $t_d$ .

To determine the time-response of the recording and analysis methods experimentally, we used a waveform generator (Agilent 33220A) to input current pulses in a method similar to Talaga and Li<sup>24</sup>. These current pulses had a  $\Delta I$  of 650 pA with a rise time of 5 ns and durations ranging from 10  $\mu$ s to 200  $\mu$ s. Analyzing the data based on the half-width of the current pulses, Fig. S19a shows that we could accurately measure the magnitude ( $\Delta I$ ) of resistive pulses if these pulses had  $t_d$  values larger than 50  $\mu$ s and Fig. S19b shows that we could accurately determine  $t_d$  values that were larger than 25  $\mu$ s. In all quantitative analyses of resistive pulses reported in this work, we constructed  $t_d$  histograms only from translocation events that lasted at least 25  $\mu$ s and  $\Delta I$  histograms only from translocation events that lasted at least 50  $\mu$ s (typically 70  $\mu$ s).

To characterize the inherent measurement error of  $t_d$ ,  $\sigma_t$ , of the recording and analysis methods, we added a current trace containing experimentally recorded electrical noise from a resistive-pulse experiment to current traces containing current pulses generated by a waveform generator. Thus, these current traces contained current pulses with a precisely defined duration

and contained a realistic representation of the electrical noise in a resistive pulses experiment. Using the resulting current traces we determined  $t_d$  based on the half-width of the current pulses as described above. For current pulses with a precisely defined duration, we measured a range of  $t_d$  values and Fig. S20 plots these values in histograms. We fit these histograms with Gaussian distributions, and from the fit we determined that the inherent measurement error of  $t_d$  ranged from 2 to 4  $\mu\text{s}$  and was not affected by the magnitude of  $t_d$ .

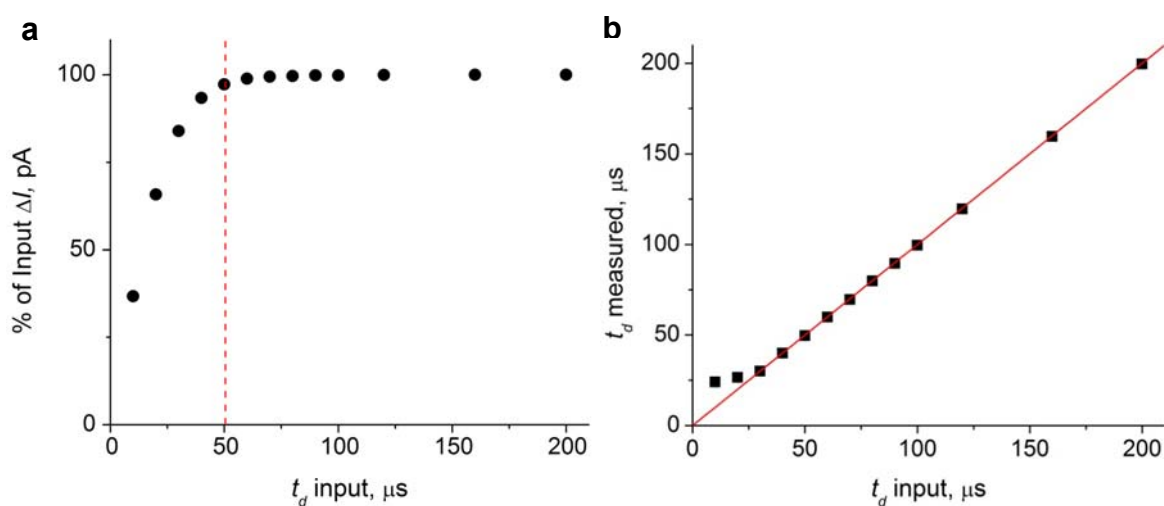


**Figure S19 | Characterization of  $t_d$  and  $\Delta I$  for pulses of various simulated translocation times resulting from an input from a waveform generator. a.** Measured values for the pulse magnitude,  $\Delta I$ , of pulses input into the headstage with a waveform generator. The dotted red line denotes the value of  $t_d$  at which  $\Delta I$  was attenuated by 3% ( $\sim 50 \mu\text{s}$ ). **b.** Measured values for the pulse duration of pulses input into the headstage with a waveform generator show that  $t_d$  could be accurately determined if it exceeded a threshold value of  $\sim 25 \mu\text{s}$ . Therefore the lower limit of accurate quantification of  $t_d$  values was  $25 \mu\text{s}$ . The red line is plotted with a slope equal to 1.

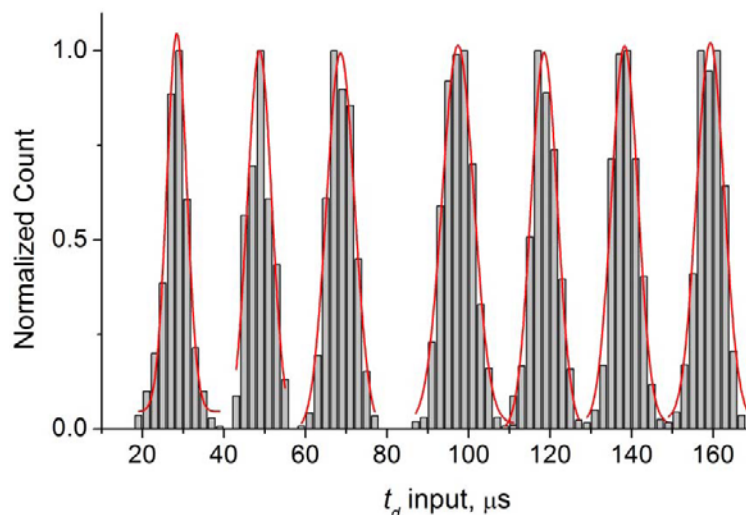


**Figure S20 | Histograms of  $t_d$  values measured from current pulses with defined duration and added electrical noise from resistive pulse experiments.** Current pulses with precisely defined durations of 30, 50, 70, 100, 120, 140, and 160  $\mu\text{s}$  were combined with electrical noise from a resistive-pulse experiment and the duration of these pulses was determined by their half-width. The red lines were obtained by fitting the histograms with a Gaussian distribution. From these fits, the measurement error of  $t_d$ ,  $\sigma_{t_d}$ , was determined to be 2.3, 4.0, 3.4, 3.9, 3.2, 3.2, and 3.4  $\mu\text{s}$  (listed in order of increasing pulse duration).

### Section S10. Preparation of Amyloid-Beta Samples and Gel-Electrophoresis

We received A $\beta$  peptides (residues 1-40, A $\beta$  1-40) in powder form from GL Biochem (Shanghai) Ltd with a purity above 98%. To remove aggregates of A $\beta$  1-40, we dissolved the powder in hexafluoroisopropanol (HFIP) to a concentration of 1 mM of A $\beta$  1-40. After 24 h incubation in HFIP, we diluted this solution with cold (4  $^{\circ}\text{C}$ ) deionized water at a 2:1 (v/v) ratio (H $_2$ O:HFIP). We then rapidly aliquoted the solution, immediately froze it in a CO $_2$ /acetone bath, and lyophilized the frozen aliquots for two days to remove HFIP<sup>39</sup>. To start the aggregation process of A $\beta$  1-40 peptides, we dissolved the lyophilized powder in deionized water to a

concentration of  $1 \text{ mg} \times \text{mL}^{-1}$ . We incubated these samples in siliconized plastic microcentrifuge tubes on a temperature-controlled shaker at a temperature of  $22 \text{ }^\circ\text{C}$ . To detect aggregates of A $\beta$  1-40, we formed a supported lipid bilayer of POPC lipids on a chip containing a nanopore with a diameter of 96 nm and a length of  $\sim 275 \text{ nm}$  (dimensions are before the lipid bilayer coating). We added solutions containing A $\beta$  1-40 to the top solution compartment of the fluidic setup such that the final concentration of A $\beta$  1-40 ranged from 0.1 to  $0.2 \text{ mg} \times \text{mL}^{-1}$ . We used a recording buffer containing 70 mM KCl and 10 mM HEPES with a pH of  $7.4 \pm 0.1$  and recorded resistive pulses at an applied potential difference of  $+0.2 \text{ V}$ .

To confirm the presence of large aggregates of A $\beta$  peptides in these samples independently, we performed a Western blot with solutions containing A $\beta$ (1-40) that were allowed to aggregate for 0, 24, 48, and 72 h. Prior to performing the electrophoresis, we followed a standard protocol<sup>40</sup> and cross-linked A $\beta$ (1-40) samples ( $1 \text{ mg mL}^{-1}$ ) with 0.04% glutaraldehyde for 20 min at room temperature and stopped the reaction by adding 200 mM of Tris. We diluted the cross-linked samples to  $0.01 \text{ } \mu\text{g } \mu\text{L}^{-1}$  in native sample buffer (Bio-Rad), containing 10% (v/v) sodium dodecyl sulfate. To resolve aggregates of A $\beta$ (1-40) of different molecular weights we used a polyacrylamide gel: 18% Tris-HCl Ready Gel (Bio-Rad) in Tris-Glycine buffer. After running the gel, we transferred proteins to a polyvinylidene fluoride (PVDF) membrane (PerkinElmer Life Science) and blocked the membrane for 1 h with TBS buffer containing 5% (w/v) nonfat dry milk and 0.0625% (w/v) Tween20. We incubated the membrane with a primary antibody against A $\beta$ (1-40) (6E10 from Covance) for 1.5 h. An IgG anti-goat antibody served as the secondary antibody and was incubated with the membrane for 1 h. We developed the membrane onto film using enhanced chemiluminescence (ECL, PerkinElmer Life Sciences). Fig. S21 shows the resulting Western blot and the increasing

molecular weights of A $\beta$ (1-40) aggregates with increasing incubation time. Note the presence of fibrillar aggregates with molecular weights greater than 250 kDa that remained in the wells of the polyacrylamide gel. Also note that the amount of these fibrillar A $\beta$ (1-40) aggregates in the wells of the gel increased with increasing time of aggregation.

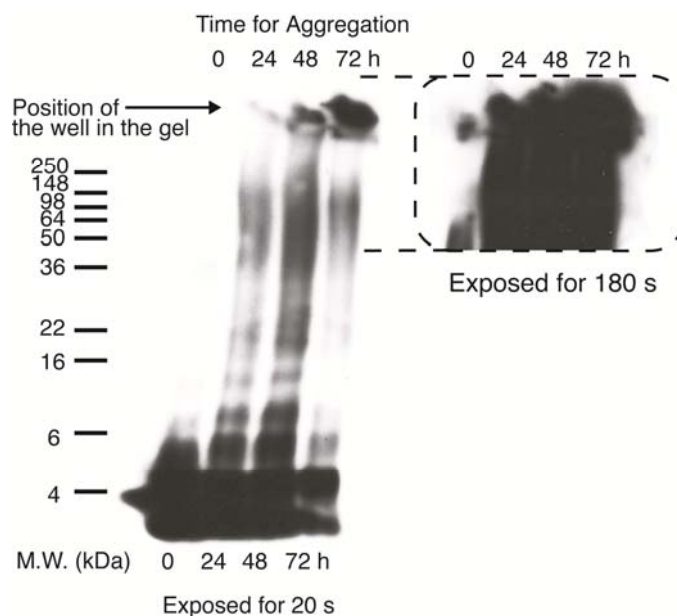


**Figure S21 | Gel electrophoresis results showing aggregation of amyloid-beta (residues 1-40) as a function of incubation time in water.** Lane 1 (0 h), containing a solution of freshly prepared A $\beta$ (1-40), shows that initially most of the A $\beta$  peptides in solution were monomers with a molecular weight of ~4 kDa. Lanes 2 (24 h), 3 (48 h), and 4 (72 h) show that as A $\beta$  aggregated in solution for increasing times, it formed aggregates of large molecular weight (6 – 250 kDa). Furthermore, lanes 2 and 3 show a population with a very large molecular weight (greater than 250 kDa) that remained in the wells of the polyacrylamide gel as it would be expected for fibrillar aggregates. The inset shows the same gel but exposed for 180 s and reveals that aggregates of large molecular weight (greater than 250 kDa), which remained in the well of the gel, were already present after 24 h of aggregation (lane 2). The molecular weight markers were SeeBlue Plus2 Stained Standard Markers from Invitrogen.



## References:

- 1 Grover, N.B., Naaman, J., Ben-sasson, S., Doljansk, F. & Nadav, E. Electrical sizing of particles in suspensions. 2. Experiments with rigid spheres. *Biophys. J.* **9**, 1415-1425 (1969).
- 2 Grover, N.B., Naaman, J., Ben-sasson, S. & Doljansk, F. Electrical sizing of particles in suspensions. I.Theory. *Biophys. J.* **9**, 1398-1414 (1969).
- 3 Hille, B. *Ion Channels of Excitable Membranes*. (Sinauer Associates, Inc., Sunderland, 2001).
- 4 Cai, Q., Ledden, B., Krueger, E., Golovchenko, J.A. & Li, J.L. Nanopore sculpting with noble gas ions. *J. Appl. Phys.* **100**, 024914 (2006).
- 5 Li, J. *et al.* Ion-beam sculpting at nanometre length scales. *Nature* **412**, 166-169 (2001).
- 6 Hamann, C.H., Hamnett, A. & Vielstich, W. *Electrochemistry*. (Wiley-VCH, New York, 1998).
- 7 Fox, R.W., McDonald, A.T. & Pritchard, P.J. *Introduction to Fluid Mechanics 6th Edition*. (Wiley, New York, NY, 2004).
- 8 Schuy, S. & Janshoff, A. Thermal expansion of microstructured DMPC bilayers quantified by temperature-controlled atomic force microscopy. *ChemPhysChem* **7**, 1207-1210 (2006).
- 9 Tokumasu, F., Jin, A.J. & Dvorak, J.A. Lipid membrane phase behaviour elucidated in real time by controlled environment atomic force microscopy. *J. Electron Microsc.* **51**, 1-9 (2002).
- 10 Reimhult, E., Hook, F. & Kasemo, B. Intact vesicle adsorption and supported biomembrane formation from vesicles in solution: Influence of surface chemistry, vesicle size, temperature, and osmotic pressure. *Langmuir* **19**, 1681-1691 (2003).
- 11 Lambacher, A. & Fromherz, P. Fluorescence interference-contrast microscopy on oxidized silicon using a monomolecular dye layer. *Appl. Phys. A-Mater. Sci. Process.* **63**, 207-216 (1996).
- 12 Saleh, B.E.A. & Teich, M.C. pg. 80 (John Wiley & Sons, Inc., 2007).
- 13 Majd, S. & Mayer, M. Hydrogel stamping of arrays of supported lipid bilayers with various lipid compositions for the screening of drug-membrane and protein-membrane interactions. *Angew. Chem.-Int. Edit.* **44**, 6697-6700 (2005).
- 14 Axelrod, D., Koppel, D.E., Schlessinger, J., Elson, E. & Webb, W.W. Mobility Measurement by Analysis of Fluorescence Photobleaching Recovery Kinetics. *Biophys. J.* **16**, 1055-1069 (1976).
- 15 Soumpasis, D.M. Theoretical-Analysis of Fluorescence Photobleaching Recovery Experiments. *Biophys. J.* **41**, 95-97 (1983).
- 16 Kalb, E., Frey, S. & Tamm, L.K. Formation of Supported Planar Bilayers by Fusion of Vesicles to Supported Phospholipid Monolayers. *Biochimica Et Biophysica Acta* **1103**, 307-316 (1992).
- 17 Starr, T.E. & Thompson, N.L. Formation and characterization of planar phospholipid bilayers supported on TiO<sub>2</sub> and SrTiO<sub>3</sub> single crystals. *Langmuir* **16**, 10301-10308 (2000).
- 18 Majd, S., Yusko, E.C., MacBriar, A.D., Yang, J. & Mayer, M. Gramicidin pores report the activity of membrane-active enzymes. *J. Am. Chem. Soc.* **131**, 16119-16126 (2009).

- 19 Hamblett, K.J. *et al.* A streptavidin-biotin binding system that minimizes blocking by endogenous biotin. *Bioconjugate Chem.* **13**, 588-598 (2002).
- 20 Janeway, C.A. *Immunobiology: the immune system in health and disease*. 5th edn, (Garland Publishing, New York, 2001).
- 21 Fein, M. *et al.* Lateral mobility of lipid analogs and GPI-anchored proteins in supported bilayers determined by fluorescent bead tracking. *J. Membr. Biol.* **135**, 83-92 (1993).
- 22 Knight, J.D. & Falke, J.J. Single-molecule fluorescence studies of a pH domain: New insights into the membrane docking reaction. *Biophys. J.* **96**, 566-582 (2009).
- 23 Gambin, Y. *et al.* Lateral mobility of proteins in liquid membranes revisited. *Proc. Natl. Acad. Sci. U. S. A.* **103**, 2098-2102 (2006).
- 24 Talaga, D.S. & Li, J.L. Single-molecule protein unfolding in solid state nanopores. *J. Am. Chem. Soc.* **131**, 9287-9297 (2009).
- 25 Redner, S. *A Guide to First-Passage Processes*. pp. 87-89 (Cambridge University Press, New York, 2001).
- 26 Wasan, M.T. *First Passage Time Distribution of Brownian Motion with Positive Drift*. pp. 6 and 15 (Queen's University, 1969).
- 27 Schneider, S.W., Larmer, J., Henderson, R.M. & Oberleithner, H. Molecular weights of individual proteins correlate with molecular volumes measured by atomic force microscopy. *Pflugers Arch.* **435**, 362-367 (1998).
- 28 Mathe, J., Aksimentiev, A., Nelson, D.R., Schulten, K. & Meller, A. Orientation discrimination of single-stranded DNA inside the alpha-hemolysin membrane channel. *Proc. Natl. Acad. Sci. U. S. A.* **102**, 12377-12382 (2005).
- 29 Akeson, M., Branton, D., Kasianowicz, J.J., Brandin, E. & Deamer, D.W. Microsecond Time-Scale Discrimination Among Polycytidylic Acid, Polyadenylic Acid, and Polyuridylic Acid as Homopolymers or as Segments Within Single RNA Molecules. *Biophys. J.* **77**, 3227-3223 (1999).
- 30 Yang, J., Mayer, M., Kriebel, J.K., Garstecki, P. & Whitesides, G.M. Self-assembled aggregates of IgGs as templates for the growth of clusters of gold nanoparticles. *Angew. Chem.-Int. Edit.* **43**, 1555-1558 (2004).
- 31 Berg, H.C. *Random Walks in Biology*. 81-84 (Princeton University Press, Princeton, NJ, 1993).
- 32 Jossang, T., Feder, J. & Rosenqvist, E. Photon-Correlation Spectroscopy of Human-IgG. *J. Protein Chem.* **7**, 165-171 (1988).
- 33 Whitlock, M.C. & Schluter, D. *The Analysis of Biological Data*. 1 edn, 33-34 (Roberts and Company, Greenwood Village, CO, 2009).
- 34 Sexton, L.T. *et al.* An adsorption-based model for pulse duration in resistive-pulse protein sensing. *J. Am. Chem. Soc.* **132**, 6755-6763 (2010).
- 35 Sivasankar, S., Subramaniam, S. & Leckband, D. Direct molecular level measurements of the electrostatic properties of a protein surface. *Proc. Natl. Acad. Sci. U. S. A.* **95**, 12961-12966 (1998).
- 36 Gitlin, I., Carbeck, J.D. & Whitesides, G.M. Why are proteins charged? Networks of charge-charge interactions in proteins measured by charge ladders and capillary electrophoresis. *Angew. Chem.-Int. Edit.* **45**, 3022-3060 (2006).
- 37 Vlasiouk, I., Kozel, T.R. & Siwy, Z.S. Biosensing with Nanofluidic Diodes. *J. Am. Chem. Soc.* **131**, 8211-8220 (2009).

- 38 Uram, J.D., Ke, K. & Mayer, M. Noise and bandwidth of current recordings from submicrometer pores and nanopores. *ACS Nano* **2**, 857-872 (2008).
- 39 Capone, R. *et al.* Amyloid-beta-induced ion flux in artificial lipid bilayers and neuronal cells: Resolving a controversy. *Neurotox. Res.* **16**, 1-13 (2009).
- 40 Stine, W.B., Dahlgren, K.N., Krafft, G.A. & LaDu, M.J. In vitro characterization of conditions for amyloid-beta peptide oligomerization and fibrillogenesis. *J. Biol. Chem.* **278**, 11612-11622 (2003).